Numerical Simulations of Flow-Induced Vibrations past a Deformable Cylinder

by

Jiajun Li

B.E., Harbin Engineering University, 2017

Submitted to the Graduate Faculty of the

Swanson School of Engineering

of the requirements for the degree of

Master of Science in Mechanical Engineering

University of Pittsburgh

2019

UNIVERSITY OF PITTSBURGH

SWANSON SCHOOL OF ENGINEERING

This thesis was presented

by

Jiajun Li

It was defended on

November 14, 2019

and approved by

Giovanni P. Galdi, Ph.D., Distinguished Professor, Department of Mechanical Engineering and Materials Science

Inanc Senocak, Ph.D., Associate Professor, Department of Mechanical Engineering and Materials Science

Hessam Babaee, Ph.D., Assistant Professor, Department of Mechanical Engineering and Materials Science

Thesis Advisor: Giovanni P. Galdi, Ph.D., Distinguished Professor, Department of Mechanical Engineering and Materials Science

Numerical Simulations of Flow-Induced Vibrations past a Deformable Cylinder

Jiajun Li, M.S.

University of Pittsburgh, 2019

When a viscous fluid flows past a blunt body at sufficiently large Reynolds numbers (Re), it naturally develops an oscillatory motion that manifests itself in the time-periodic variation of the wake behind the body, a von Karman vortex street (VKVS). If the body is elastic, the frequency of the oscillations may be close to the natural frequency of the body, thus producing a resonance phenomenon that can lead to catastrophic consequences. A remarkable example is the collapse of the Tacoma Narrows Bridges.

Traditionally, most numerical simulations and experiments are flow past a rigid body. In this thesis, the ANSYS Workbench coupling system was used to investigate this question in the care of an elastic body in the shape of a cylinder (FSI) clamped at both ends. We modeled the cylinder as silicon rubber to allow sufficiently large deformation even at small Reynolds numbers. This simulation starts from a relatively low Reynolds number (Re100) up to a medium-range of values (Re2000). Results are compared with flow past a rigid cylinder, and it turns out that quite different phenomena are observed. The deformable cylinder prevents or mitigates vortex shedding to some degree. Besides, bifurcation patterns are varying from those observed in rigid ones. Drag and lift coefficients and displacements plots specifically demonstrate the occurrence of the phenomena. Deep understandings of such phenomena may improve configurations of architectures to avoid flow-induced vibrations and vortex-induced vibrations (VIVs).

Keywords: Vortex shedding, fluid-structure interaction, vortex-induced vibrations, bifurcations.

Table of Contents

List of Tables

List of Figures

Preface

I investigated fluid-structure interaction for Dr. Giovanni Paolo Galdi from January 2019 to November 2019. After months of investigation, we found an interesting phenomenon—different bifurcations occur when fluid flows over a deformable cylinder, which may be used to avoid Karman vortices affecting architecture. Professor Galdi provided excellent help, including academic instructions and technical supports. Thanks to the Center for Research Computing and Dr. Shervin Sammak, I completed the calculations in time. ANSYS® Workbench™ software is convenient and gives promising results. Also, Libby Ferda from the Writing Center provided a significant contribution to the revision.

Nomenclature

Re—Reynolds number

VKVS—Von Karman vortex street

VIVs—Vortex-induced vibrations

FSI—Fluid-structure interaction

Cd—Drag Coefficient

Cl—Lift Coefficient

St—Strouhal number

Mass ratio—$m^* = \frac{m}{\pi \rho D^2 L/4}$

m—The mass of the cylinder

ζ—Damping ratio

c—Damping coefficient

k—Stiffness

D—The diameter of the cylinder

ρ—The fluid density

1.0 Introduction

Vortex-induced vibration (VIV) occurs when shedding vortices (a von Karman vortex street) exert oscillatory forces on a cylinder in the direction perpendicular to both the flow and the structure. The structure starts to oscillate due to these forces if it is not fixed. For fixed cylinders, the vortex-shedding frequency is related to the non-dimensional Strouhal number. Strouhal number is defined as $St = f_v D/U$; where f_v is the predominant frequency of vortex shedding. U is the steady velocity of the flow, and D is the diameter of the cylinder. Strouhal number is found to be nearly constant, with a value of 0.2 for an extensive range of Reynolds numbers. This range is often called the subcritical range and spans the Reynolds number range of $300 - 2 \times 10^5$ (Grunwald, 1989).

For flow past cylinders that are free to vibrate, the phenomenon of synchronization or lock-in is observed. For low flow speeds, the vortex-shedding frequency f_v will be the same as that of a fixed cylinder. This frequency is fixed by the Strouhal number. As the flow speed is increased, the shedding frequency approaches the vibration frequency of the cylinder f_0: In this regime of flow speeds, the vortex-shedding frequency no longer follows the Strouhal relationship. Instead, the shedding frequency becomes "locked-in" to the oscillation frequency of the cylinder (i.e., $f_0 \approx f_v$). If the vortex-shedding frequency is close to the natural frequency of the cylinder f_n, as is often the case, large body motions are observed within the lock-in regime (the structure undergoes near-resonance vibration) (Gabbai & Benaroya, 2005).

While the dynamics of VIVs is our main concern, it is of basic interest to understand the creation of the wake structure as Re is increased from very low values. According to Williamson (1996) and Coutanceau & Defaye (1991), for the flow around a circular cylinder, the process is

1

well described: For Re < 5 the flow is attached to the cylinder, and for 5 < Re < 45 two steady counter-rotating vortices exist behind the cylinder. At Re = 45, the flow becomes unsteady in a Hopf bifurcation, and one enters the vortex-shedding regime. Hence, in the early stages of the wake development, there are two basic bifurcation phenomena occurring: A topological bifurcation at Re = 5, where the steady flow field changes its topology but not its stability, and a dynamic bifurcation at Re = 45 where a new family of periodic flows is created.

There are numerous experimental studies on the vortex-induced vibration of bluff bodies, especially circular cylinders. These studies have examined a multitude of phenomena, from vortex shedding from a stationary bluff body to vortex shedding from an elastic body. The vibration caused by vortices generated by the flow past a structure depends on several factors. The correlation of the force components, the shedding frequency, the Reynolds number, the material damping and structural stiffness of the cylinder, and the added mass effect are just a few of these (Gabbai & Benaroya, 2005).

According to Navrose & Mittal (2016), lock-in/synchronization/wake-capture is an important phenomenon associated with vortex-induced vibrations of bluff bodies. It is characterized by a high amplitude of structural vibrations. These vibrations can cause fatigue and may lead to catastrophic failure of structures. Lock-in, therefore, has been a subject of numerous computational and experimental studies in the past. The vortex shedding frequency of the cylinder changes to match the frequency of the cylinder motion (Schulz & Kallinderis, 1998). When this synchronization occurs, the phenomenon is deemed lock-in since the vortex shedding no longer occurs at the natural shedding (Strouhal) frequency (Yeung & Vaidhyanathan, 1993).

It was found that small pre-strain would suppress the VIVs of 2D membrane wing when the attack angle was equal to zero (Sun, Wang, Zhang, & Ye, 2018). In Figure 1, the "bumpy"

cylinder provides vortex-induced vibration (VIV) suppression (Owen, Bearman, & Szewczyk, 2001).
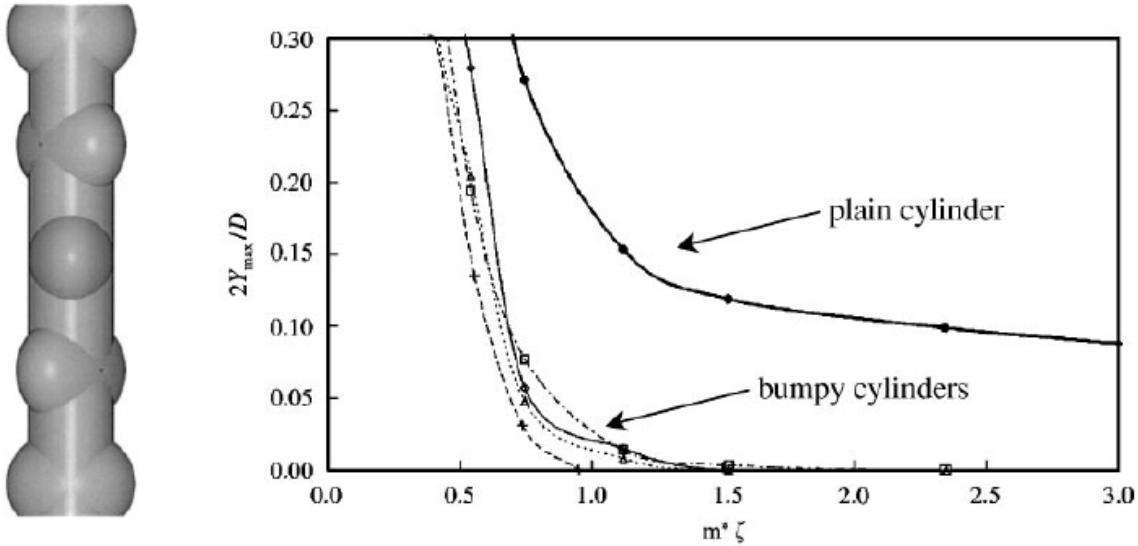

Figure 1. Bumpy cylinders versus plain cylinders. $m^* = 4m/\pi\rho D^2 L$; damping ratio $\zeta = c/2\sqrt{k(m + m_A)}$; Y_{max}—maximum transverse displacements; D—diameter of the plain cylinder

Investigations to suppress VIV stemmed from the original work of Tombazis & Bearman (1997) and Bearman & Owen (1998), where they investigated the influence of an imposed spanwise waviness of the flow separation lines around bluff bodies. They achieved a drag reduction of 30% and a suppression of classical vortex shedding. A principal idea is to weaken vortex shedding without the drag increase associated with traditional "helical strakes"(Zdravkovich, 1981). Subsequently, Owen studied the effects of a sinuous waviness on the axis of a cylinder, as well as the effects of introducing hemispherical bumps to the cylinder surface, which yield an encouraging 25%~47% reduction in drag (Owen et al., 2001).

There was a popular belief at the time that Reynolds number plays a minor role and that the flow around a cylinder undergoing large vortex-induced vibrations is insensitive to Reynolds

number changes (Griffin, Skop, & Ramberg, 1975). However, Klamo et al. (2005) and Govardhan & Williamson (2006) have both since demonstrated the strong influence of Reynolds number on the maximum response of a cylinder as the Reynolds number range of available data has increased.

As for industrial applications, for example, as A.D. Trim et al. (2005) said, there is a considerable disparity between predictions of marine riser VIV fatigue damage, and often the agreement between computer models and observed VIV-related damage is inaccurate by orders of magnitude. Resulting problems for deepwater riser design are the need for large safety factors on fatigue damage predictions and the use of expensive vortex-suppression devices. The results suggest that a key consideration in VIV fatigue design is the length of suppression coverage and the nature of the flow to which the bare section of the riser is exposed

There are also other journal articles concerning different CFD algorithms or deep learning stuff, such as numerically investigated dynamics of a pressurized elastic ring pinned at one point within a uniform flow by using an immersed-boundary algorithm (Shoele & Zhu, 2010); the prediction of the lift and drag forces on the structure gives some limited and scattered information on the velocity field (Raissi, Wang, Triantafyllou, & Karniadakis, 2019).

Three dimensional Navier-Stokes equations, matrices of beam element arbitrarily oriented in space, and stress analysis are elaborately illustrated in the following references: fundamental mechanics of fluids (Currie, 2003, pp. 32-33) and Finite Element Method (Logan et al., 2007, pp. 255-260, pp. 490-493).

2.0 CFD Preprocessing

In ANSYS® Academic Research Workbench, Release 19.2, as shown in Figure 2, Tansient Structural and Fluent are coupled to simulate a fluid flows past a deformable cylinder marching time.
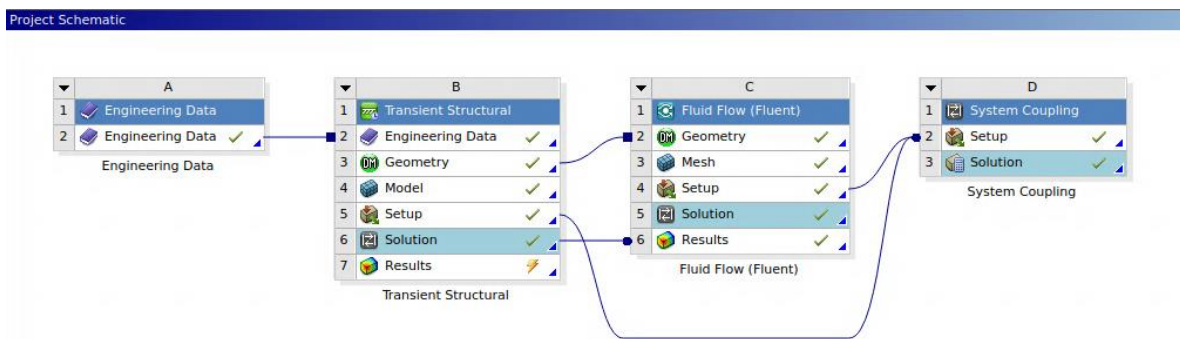

Figure 2. The project schematic

2.1 Engineering data

Before the simulation design, it is significant to consider what phenomena and experimental requirements are expected to avoid troubles and undesirable results. First of all, laminar flow and low Reynolds numbers are flow characteristics that are expected. Secondly, large deformation is helpful to investigate the mechanism of fluid-structure interaction, fatigue, and failure. As a result, silicon rubber is an ideal material to meet the previous requirements. Properties of silicon rubber are listed below.

Table 1 Properties of silicon rubber

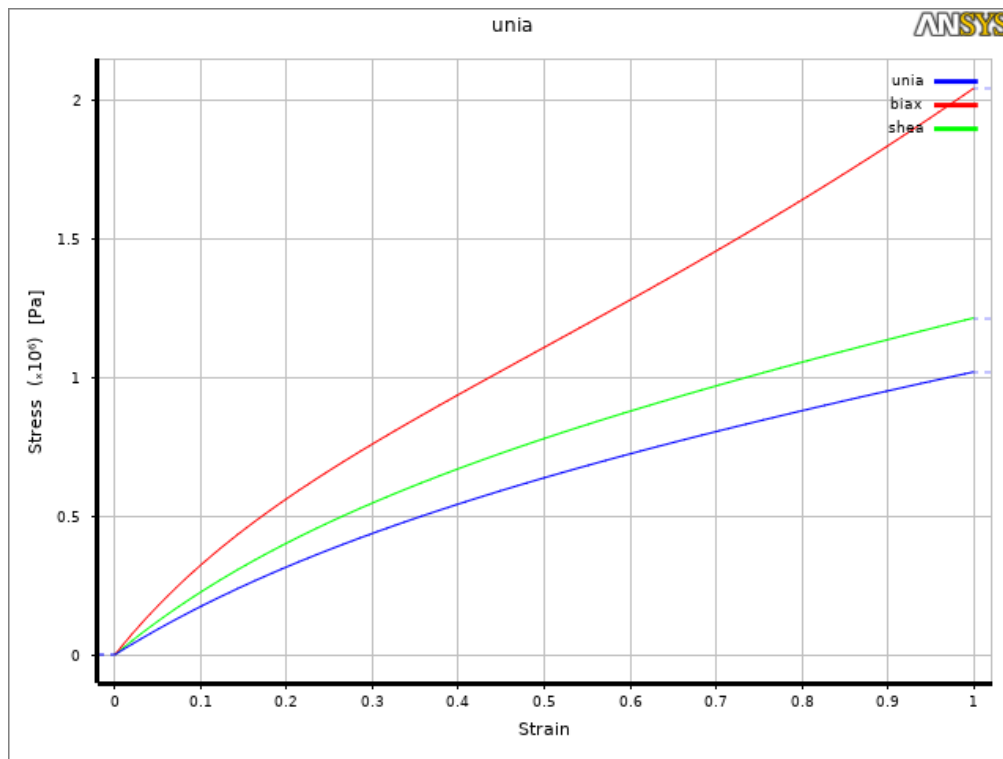| Property	Value	Unit
Density	1120	$kg \cdot m^{-3}$
Isotropic Secant Coefficient of Thermal Expansion		
Coefficient of Thermal Expansion	0.000274	C^{-1}
Mooney-Rivlin 2 Parameters		
Material Constant C10	2.59E + 05	Pa
Material Constant C01	65000	Pa
Incompressibility Parameter D1	1.14E − 09	Pa^{-1}
Tensile Yield Strength	8.97E + 06	Pa
Tensile Ultimate Strength	8.97E + 06	Pa

Figure 3. Mooney-Rivlin 2 parameter

2.2 Geometry

As shown in Figure 4, the fluid domain is 15 meters long, 8 meters high, and 10 meters wide. The cylinder is 10 meters long, with 0.5 meters' diameter. Thus, the flow dynamics is sufficiently developed across the length L of the computational domain. Because the top and bottom boundary effects may influence the flow passing over the cylinder, the height H of the domain needs to be prescribed at a distance to sufficiently remove any of these boundary effects on the fluid flow surrounding the cylinder but still be manageable for CFD calculations (Tu, Yeoh, & Liu, 2018).
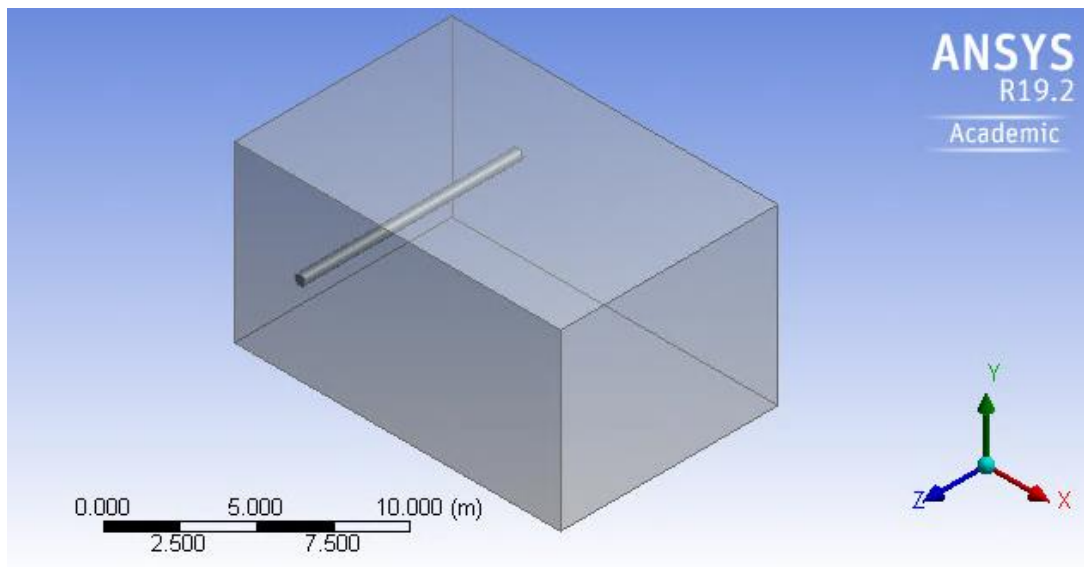

Figure 4. The geometry of fluid and structure domain

2.3 Computational Mesh

For the structural part, it is divided into 7500 cells. The sweep method is used to mesh a regularly shaped object. The maximum skewness is 0.4, and the average skewness is 0.27, while the min orthogonal quality is 0.66, and the average is 0.94. Both the skewness and the orthogonal quality show a good meshing, as shown in Figure 5.
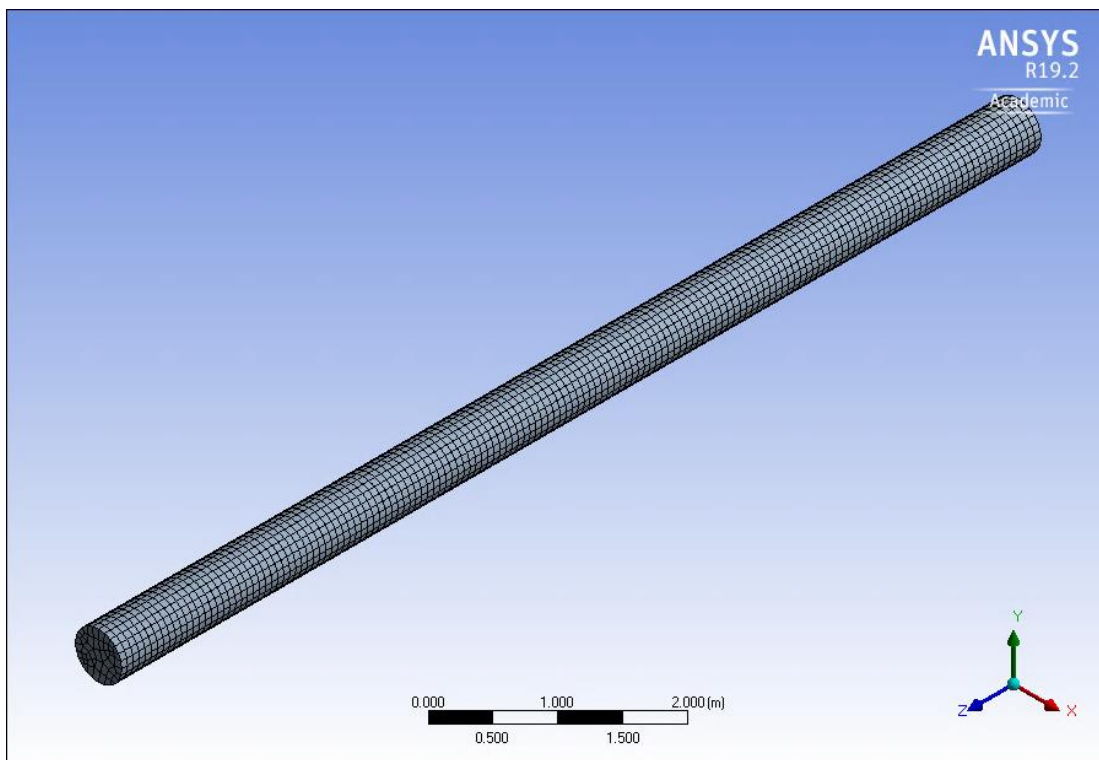

Figure 5. Cylinder meshes

As for fluid, 480,000 cells are generated (the default element size is 0.2 m). Round-off error plays an essential role in numerical accuracy, and thousands of timesteps would enlarge such an error. Additionally, small timesteps and fine meshes are crucial to accuracy. Thus, the balance between round-off and truncation errors is a choice to minimize total error. As shown in Figure 6, inflation and face sizing are used to capture the detailed information of vortices shedding around

the cylinder. The inflation option is first layer thickness, and the first layer height is 0.01 m. The growth rate is 1.1, and the maximum number of layers is 10. As for face sizing, the element size is 0.1 m. The maximum skewness is 0.79 (<0.85), and the average skewness is 0.22, while the min orthogonal quality is 0.21 (>0.1), and the average is 0.78.
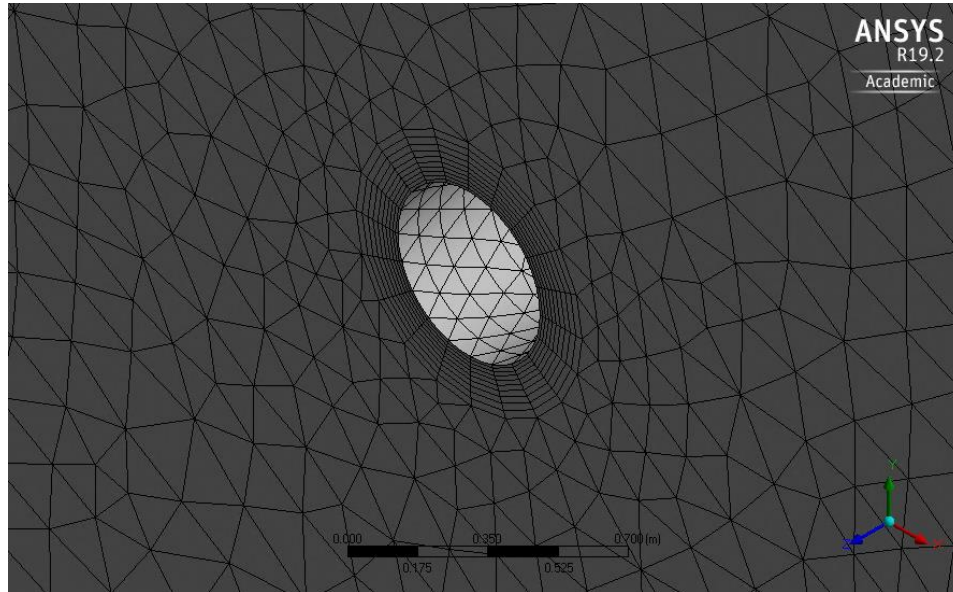

Figure 6. Zoomed-in fluid meshes

In Figure 7, name selections are created to mark different boundaries for further setting up the software environment. The inlet is the velocity input, and the outlet is the velocity output (outflow). The top and bottom surfaces of the cylinder are fixed, while the side face is the fluid-solid interface for FSI data transfer. The other boundary conditions are set to be symmetrical.
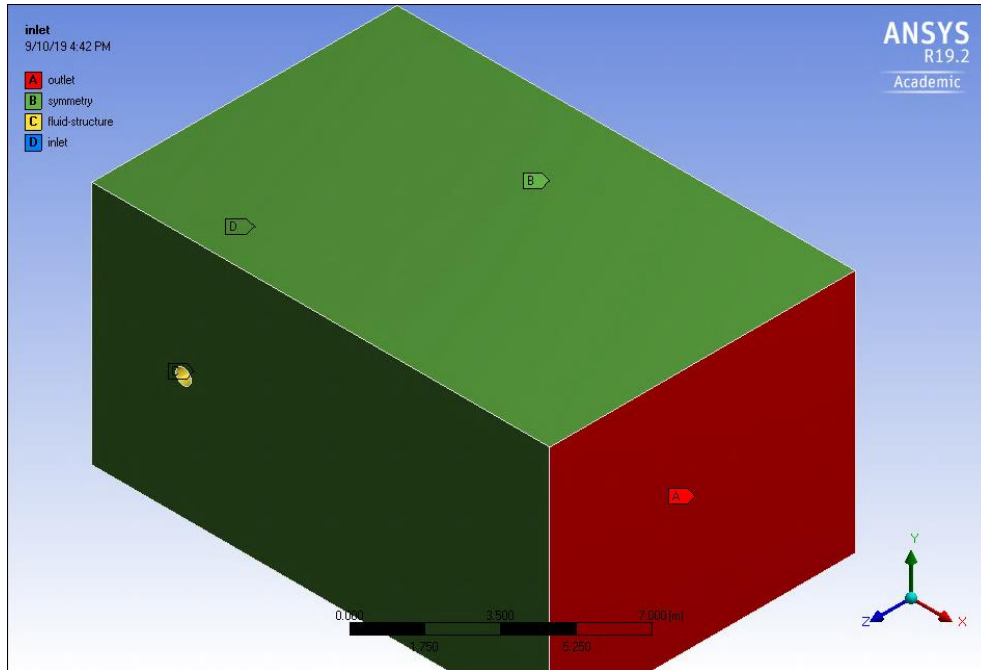
Figure 7. Named selections

2.4 Setup

Karman vortex shedding is a transient simulation, and the Reynolds number is small, so the viscous model is set as laminar flow. Low mass ratio cylinders have lock-in regions that extend over a broader range of flow speeds. Cylinders with high mass ratios show smaller increases in natural frequency with variations in added mass (Vikestad, Vandiver, & Larsen, 2000). Fluid density is $1000 \ kg/m^3$ as a liquid, and viscosity is $2 \ kg \cdot m^{-1}s^{-1}$. For dynamic mesh, smoothing, layering, and remeshing are used, including linearly elastic solid method, local cell, local face, region face, and cutcell zone. Poisson's ratio is 0.48. In dynamics mesh zones, system coupling is selected for the fluid-structure interface.
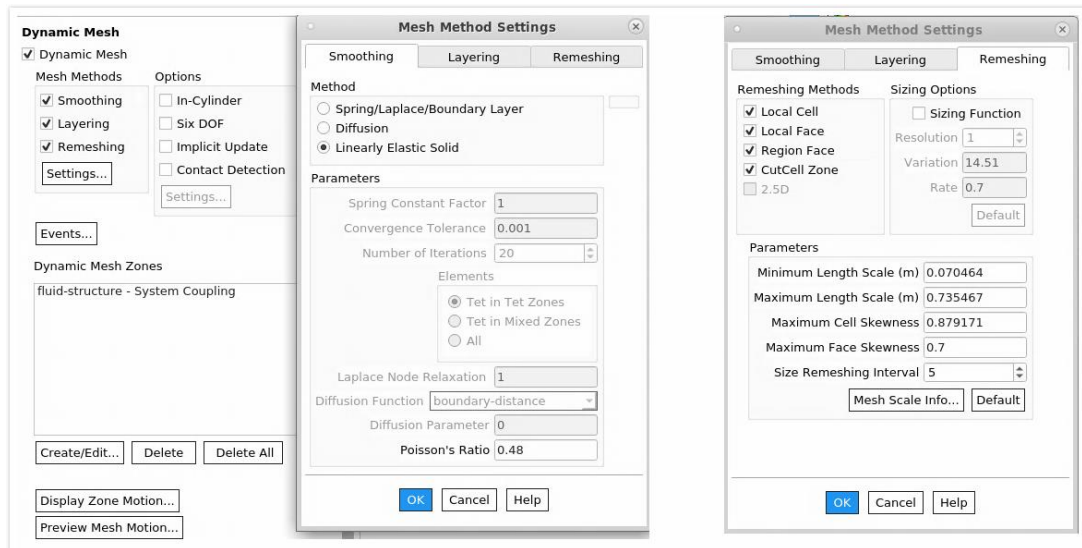
Figure 8. Dynamic mesh settings

Fluid-structure interaction is a time-consuming simulation because of the dynamic mesh and coupling system data transfer. On the one hand, the deformation of the cylinder is quick, and a small timestep is preferred. On the other hand, a VKVS is a relatively long timespan process. Thus, the balance between accuracy and calculation duration is essential. The time step is 0.03 seconds, and the total time is 30 seconds, except for the Re=100 (60 seconds). Max iterations per time step are 35. In residual monitors, we set continuity and x, y, and z velocities absolute convergence criteria to 1×10^{-6}. For accuracy and to reduce simulation time, the second-order implicit method is used. After hybrid initialization, the calculation is ready. We save the project, sync workbench, and then go to the coupling system.

In analysis settings, we put end time, step size, and maximum iterations as mentioned before, and then create data transfer between transient structural and fluid. Intermediate restart data output shows the frequency of saved files. Last but not least, we go to the solution and update.

A vortex street will form at a specific range of flow velocities, specified by a range of Reynolds number, typically above 90 (40–60 for 2D). To make precise comparisons, five

11

simulations in which Reynolds numbers 100, 300, 500, 1000, and 2000 are selected to give a general conclusion. Viscosities among Re100, 300, and 500 are the same ($2\ kg \cdot m^{-1} \cdot s^{-1}$), and the variable is velocity. However, viscosities among Re500, Re1000, and Re2000 are different, and velocities are the same ($2\ m/s$) to avoid overlarge deformation that may shut down the solver.

3.0 Post-processing

3.1 Fluid-Structure Interaction

Fluid-structure interactions (FSIs) are frequently encountered in many areas, ranging from the traditional automobile and airplane industries to the relatively newer field of biomechanics. The dynamic response of the structure is stimulated by the periodic or random FSI force from the FSI interface partially induced by the vortex shedding of the fluid flow (Wang, Khoo, Liu, Xu, & Chen, 2014).

3.1.1 Reynolds number of 100

In our FSI simulations, due to the drag force, the cylinder begins to bend at first, and then the wake stretches before oscillating. Vortices shed, and the cylinder starts (at 20 seconds) to vibrate violently, and the maximum displacement occurs at the middle plane of the cylinder. Figure 9 illustrates the deformation of the cylinder and wake oscillations.

As seen in Figure 10, in the transverse direction, the cylinder swings up and down. It is reasonable because Karman vortex shedding makes periodic pressure changes.
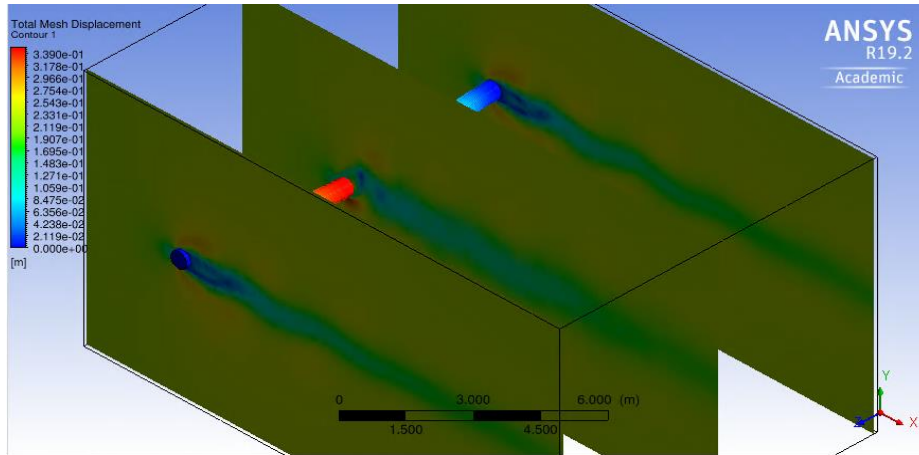
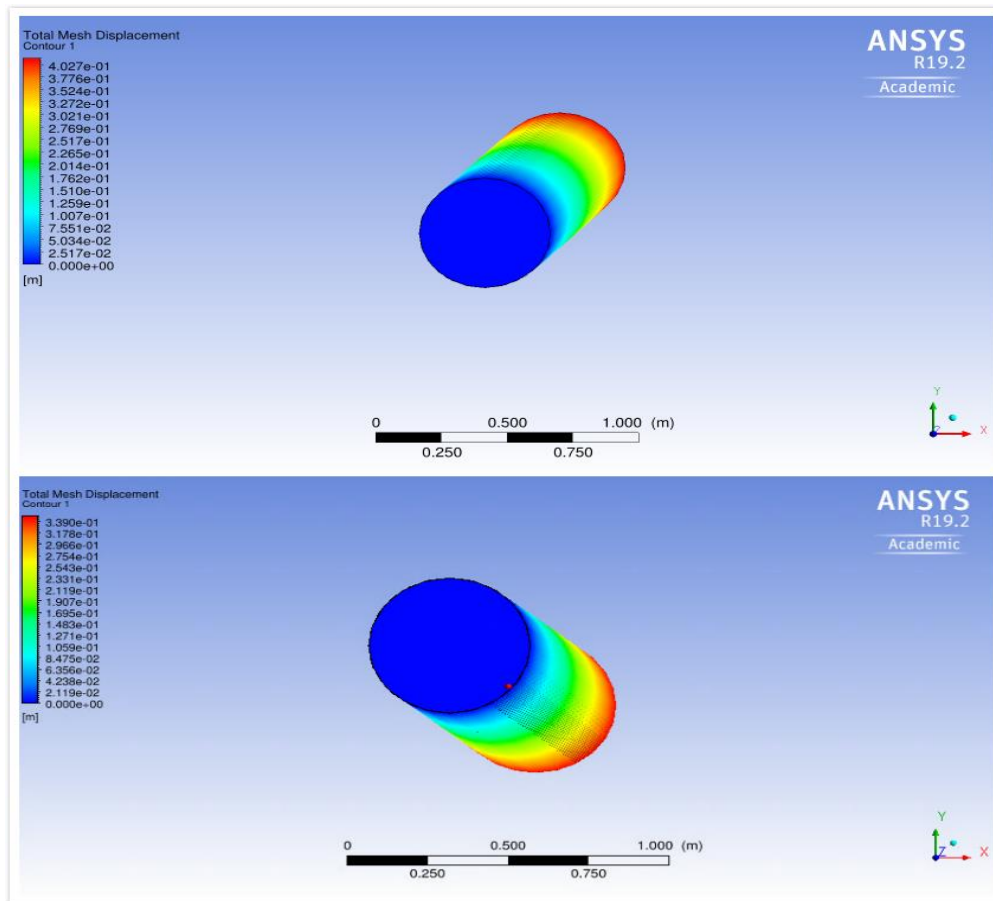**Figure 9. Vortices shedding and cylinder deformation**

Figure 10. The cylinder swinging of Re100

3.1.2 Reynolds number of 300

Karman vortices shed after the cylinder bends to a stable deformation. However, it is not the end, and the cylinder begins (at 7 seconds) to oscillate and distort to high magnitude. The differences between cases Re100 and Re300 are that in the former one, the cylinder's vibration is more considerable while the latter's deformation is more significant. Most importantly, the cylinder not only swings but distorts, as shown in Figure 11, which attributes to different sections' varying periodic pressure changes.
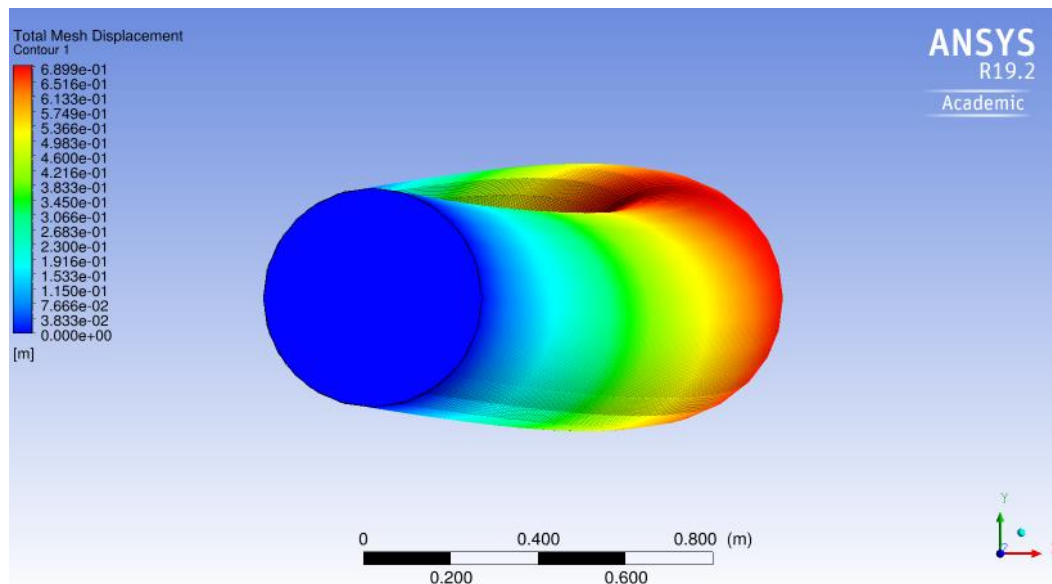

Figure 11. The cylinder distortion of Re300

Further investigations of vibration frequencies and amplitudes are shown in Figures 12–14. We choose the center of the middle longitudinal section of the cylinder to study its motion. First, in-line displacements of Re300 are significantly larger than that of Re100, but Re100 has exceedingly huge transverse displacements. It is reasonable that the increase in speed makes a larger drag force that causes larger deformation. As for the transverse

displacements, there are two possible reasons: the large pre-strain mitigates the transverse vibrations, or resonance brings different effects on Re100 and Re300.
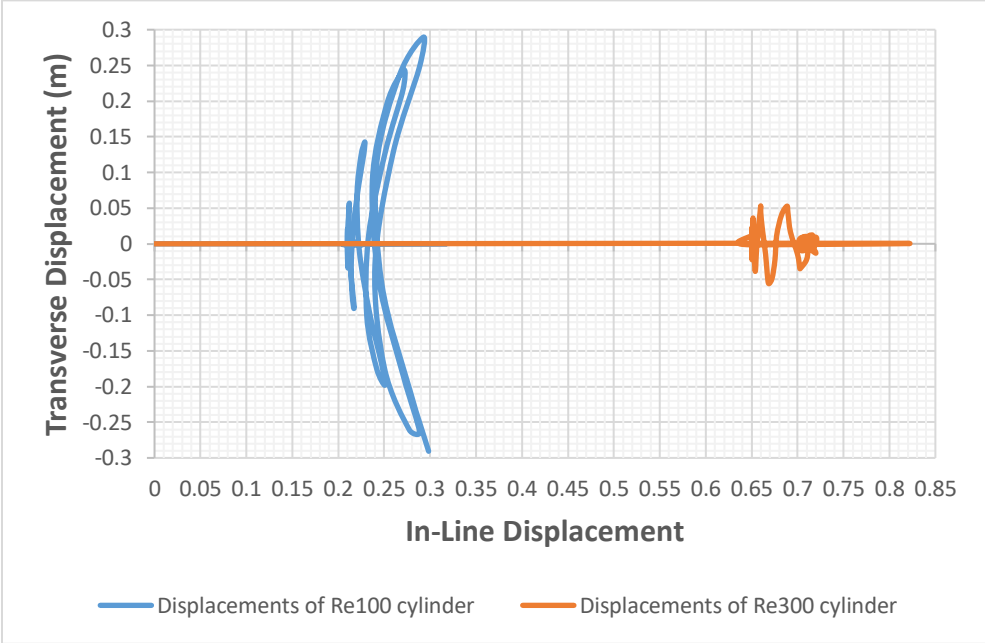

Figure 12. Overall displacements history of Re100 and Re300

Figures 13 and 14 illustrate the fluctuations of transverse displacements and in-line displacements of Re100. Both fluctuations are higher than those of Re300. The pre-strain of Re300 might decrease further in-line displacements, but it would not be helpful in transverse transformation. Thus, resonance is likely the reason why large Reynolds numbers do not bring vibrant vibrations. It is important to clarify that even though the maximum displacement is 60%–140% of the cylinder diameter, the maximum strain is smaller than 0.12. As listed before, in Figure 3, the whole deformation can be seen as linear.
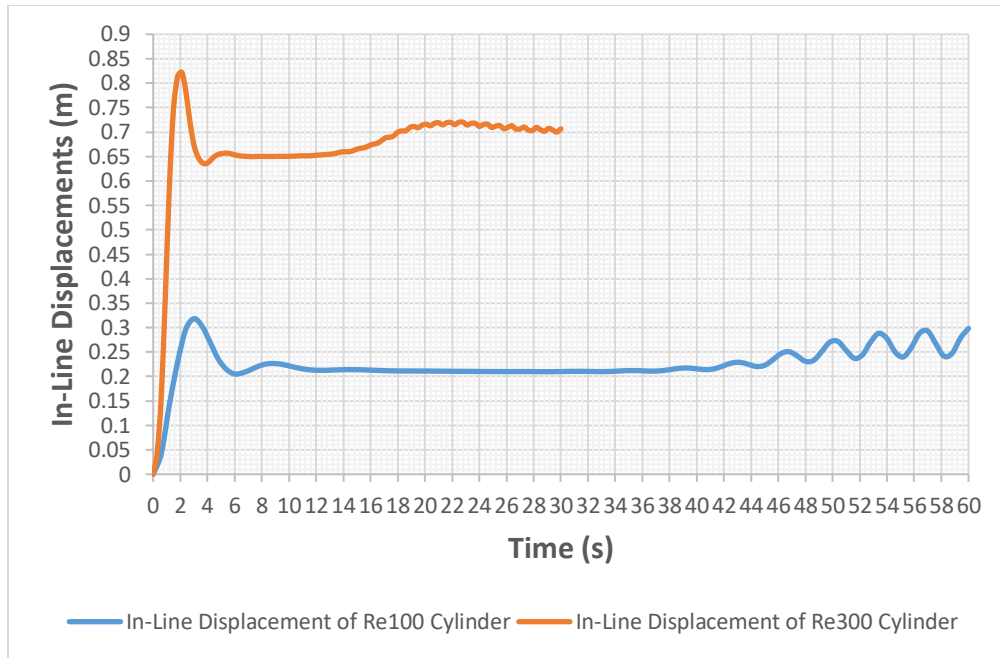
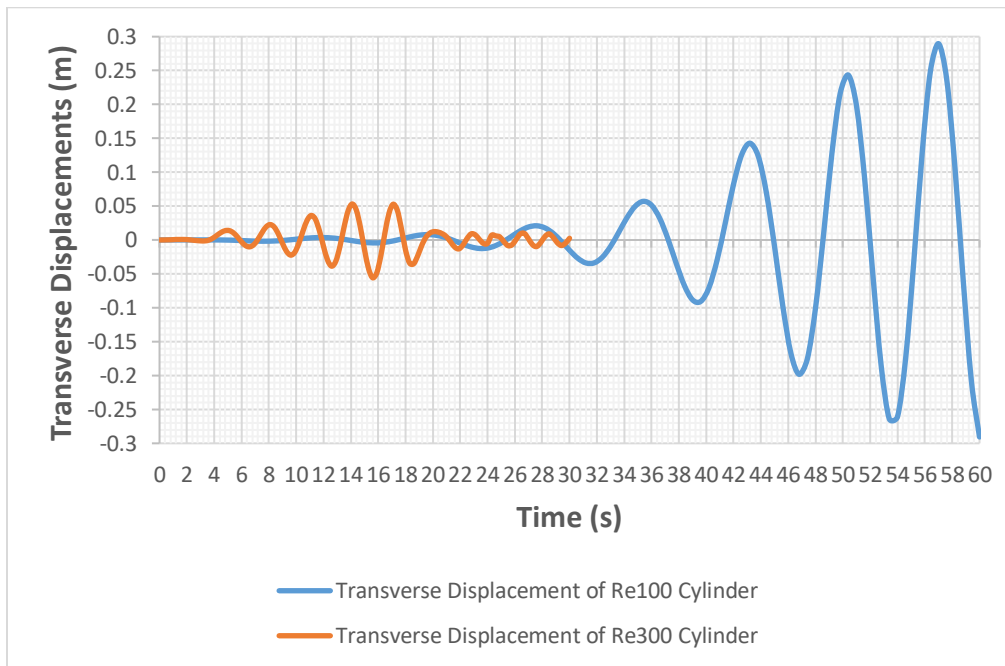**Figure 13. Re100 and Re300 in-line displacements versus time**

Figure 14. Re100 and Re300 transverse displacements history versus time

17

In general, the strain is under 0.12. Based on Figure 2, the deformation can be assumed to be linearly elastic, so Young's Modulus is approximately 1.8 MPa. Additionally, the cylinder's density is $1120\ kg \cdot m^{-3}$, and the cylinder is fixed at each end. We put those parameters in the modal of ANSYS workbench, and the cylinder's first natural frequency turns to be 0.179 Hz, and mode 2 is 0.484 Hz.

The vortex shedding frequency of an infinite cylinder is given by $f = \frac{US_r}{L}$. Because of the large aspect ratio ($L/D = 20$), this formula is applicable. The theoretical vortex shedding frequencies of Re100, Re300, Re500, Re1000, and Re2000 should be 0.128 Hz, 0.432 Hz, 0.8 Hz, 0.86 Hz, and 0.86 Hz respectively. Recall that velocities are the same for the last three cases, and viscosities are the same for the first three ones. Results show that vortex shedding frequencies of Re100 and Re300 are 0.133 Hz and 0.333 Hz. That is exactly a "lock-in" effect, which means vortex-induced vibrations perfectly coincide with vortex shedding. The vortex shedding frequency of Re100—0.133 Hz is closer to the first natural frequency 0.179 Hz, while the vortex shedding frequency of Re300—0.333 Hz is between the first natural frequency 0.179 Hz and the second natural frequency 0.484 Hz. From the resonance perspective, it makes sense that the vibration amplitude of Re100 is higher than that of Re300.

3.1.3 Reynolds number of 500

Nevertheless, when the Reynolds number is 500, both structure and flow are almost stable. After zooming in the velocity field, 94% of fluid domain, from 0.3 meters wide to 9.7 meters wide, is steady. Even in the area out of this domain, the wake is almost steady, as shown in Figure 15. It makes sense that the cylinder does not vibrate but converges to a steady deformation, as demonstrated in Figure 16. It is a counterintuitive result because larger velocity vortices should shed quickly and wildly, and so do the cylinder oscillations. There must be some unique characteristics of Re500 that mitigate or even prevent Karman vortex shedding.
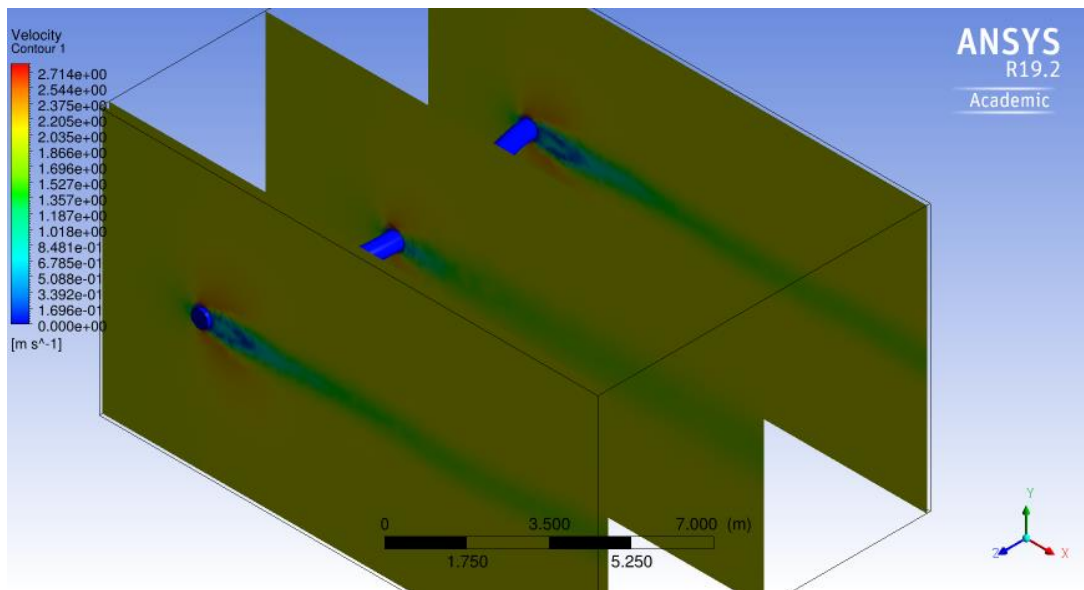

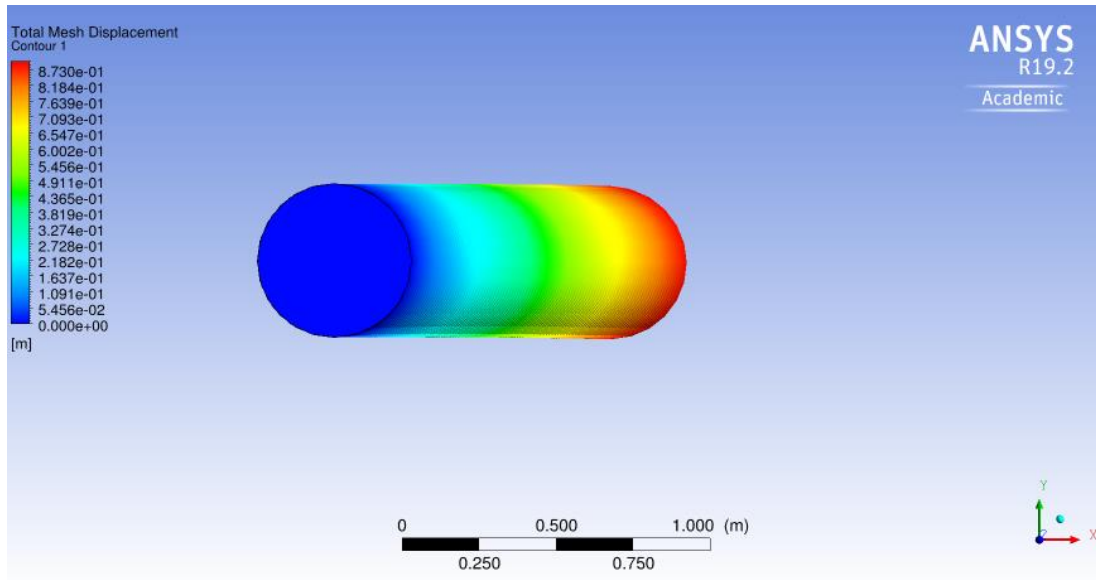**Figure 15. The almost steady-state domain of Re500**

Figure 16. The steady deformation of Re500

3.1.4 Reynolds numbers of 1000 and 2000

Reynolds numbers 1000 and 2000 are different from Re500 because there is less domain close to both the cylinder ends are steady (86% and 80%). For simplicity, only the plot of the Re1000 steady flow is presented in Figure 17. The previous results include the FSI simulation, and the bifurcation occurs as the Reynolds number changes. There are tiny oscillations that must be viewed by video for case Re2000 and can be demonstrated later in Figure 24. Compared with flow past a rigid cylinder Re1000 and Re2000, frequencies of vortex shedding in FSI cases are lower. In Figure 18, vortex shedding is not continuous, and there is a pause between two vortices shedding, while vortex streets of the rigid cylinder are continuous in Figures 20 and 21. In other words, vortex streets are prevented or mitigated by the deformable cylinder.

As shown in Figures 20 and 21, if the cylinder is rigid, the fluid domain is transient in all of these Reynolds numbers. The Karman vortex is periodic for these Reynolds numbers.
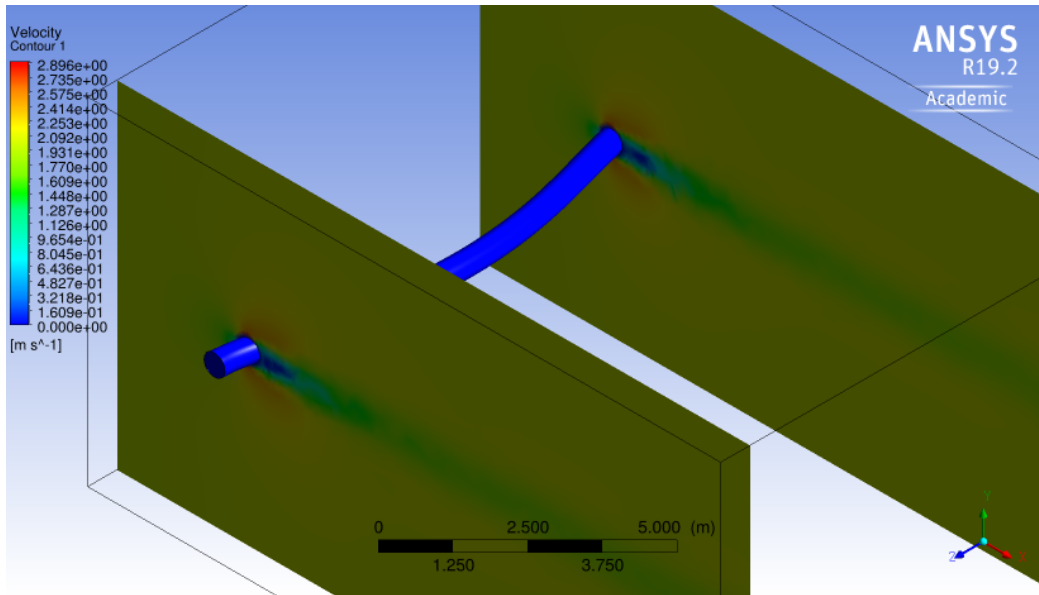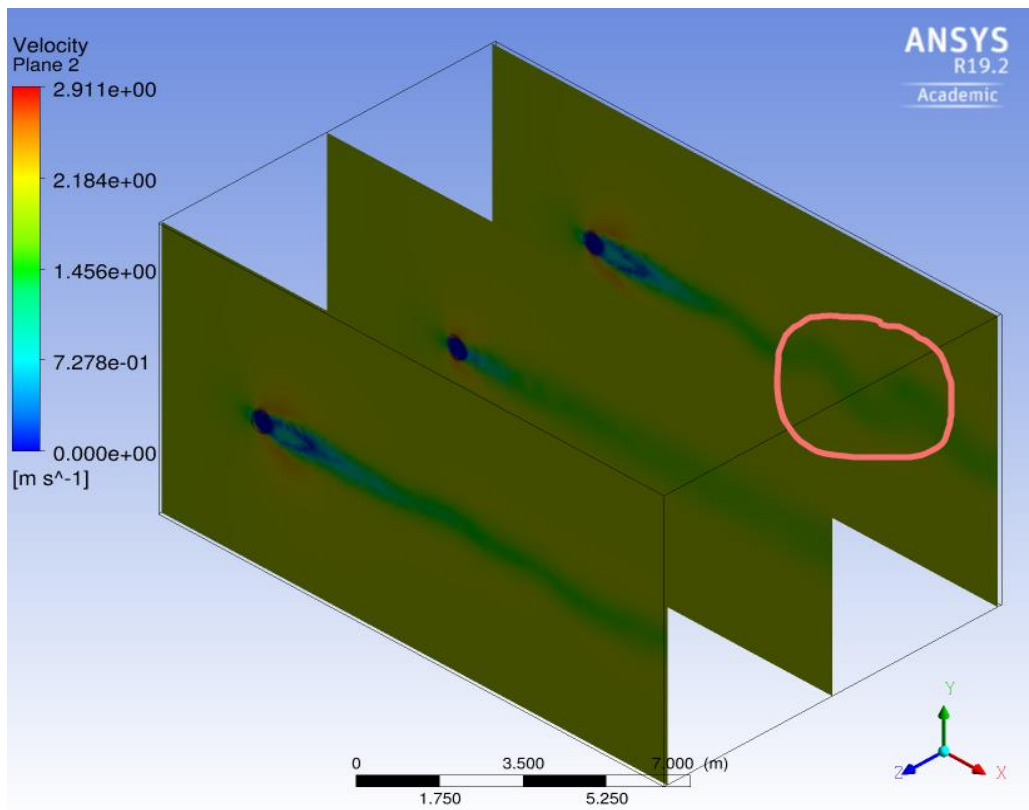
Figure 17. Re1000 FSI Steady Domain
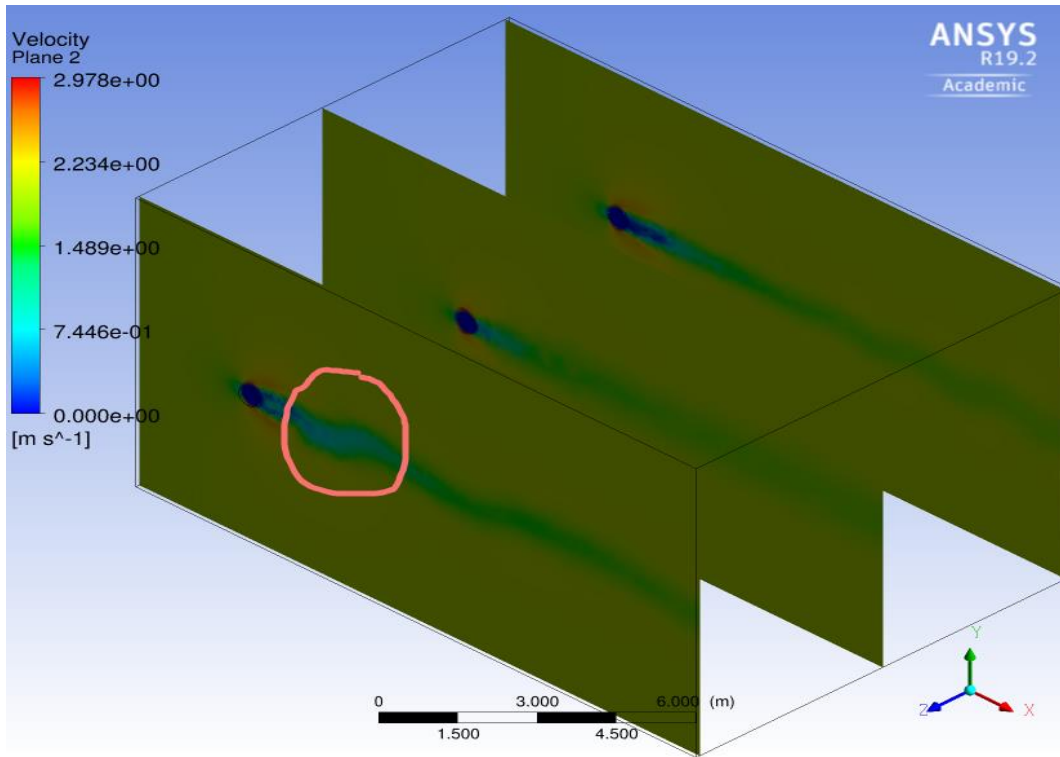

Figure 18. Re1000 FSI discontinuous vortex shedding

21

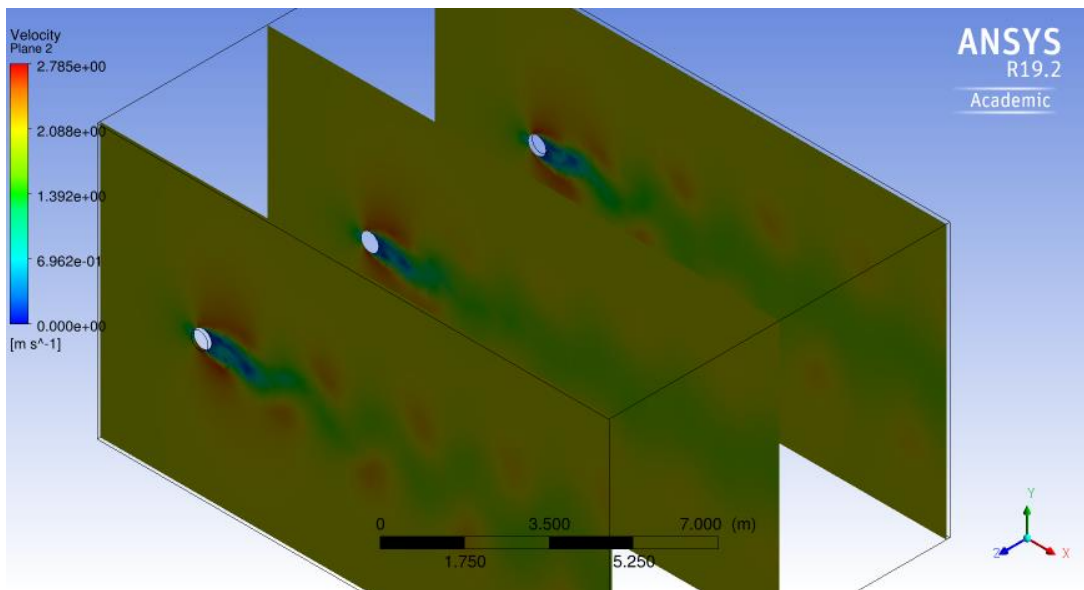**Figure 19. Re2000 FSI discontinuous vortex shedding**

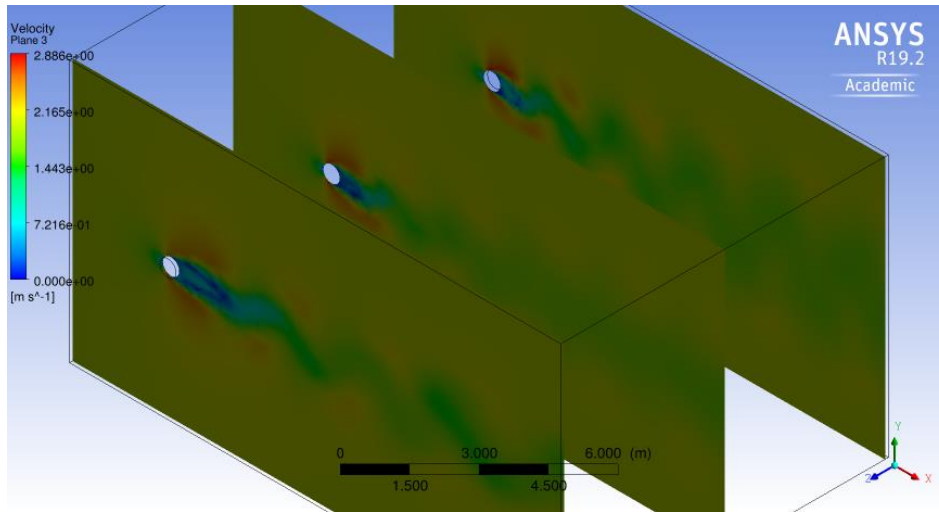**Figure 20. Re1000 Rigid regular cylinder vortex shedding**

Figure 21. Re2000 Rigid regular cylinder vortex shedding

Figure 22 shows the total displacements history of these three groups. Comparisons of displacements under three Reynolds numbers are listed next. As seen in Figure 23, the line of the Re500 is the most straight, and there are fluctuations in the curves of Re1000 and Re2000. Unlike the results of Re100 and Re300, those three groups converge even though there are small irregular fluctuations in Figure 24, which confirms the vibrations of Re2000 seen in animations by the naked eye. It seems like the transverse displacement should be zero because the cylinder is symmetrical. But the exact cylinder is not perfect due to finite meshes, and there is no perfect cylinder in nature. And, different Reynolds numbers may amplify such imperfection and bring varying results. It is like tossing a coin, 50/50 chance. It does not matter because the transverse displacements are far smaller than in-line displacements; thus, the cylinder can be seen at the balance place.

In Figure 24, The transverse displacements curves of Re1000 and Re2000 are not sinusoidal, which explains the discontinuous vortex shedding in Figures 18 and 19. From the energy perspective, such discontinuity is another rhythm of energy accumulation and release that is different from the usual sinusoidal way of flow past a rigid regular cylinder.
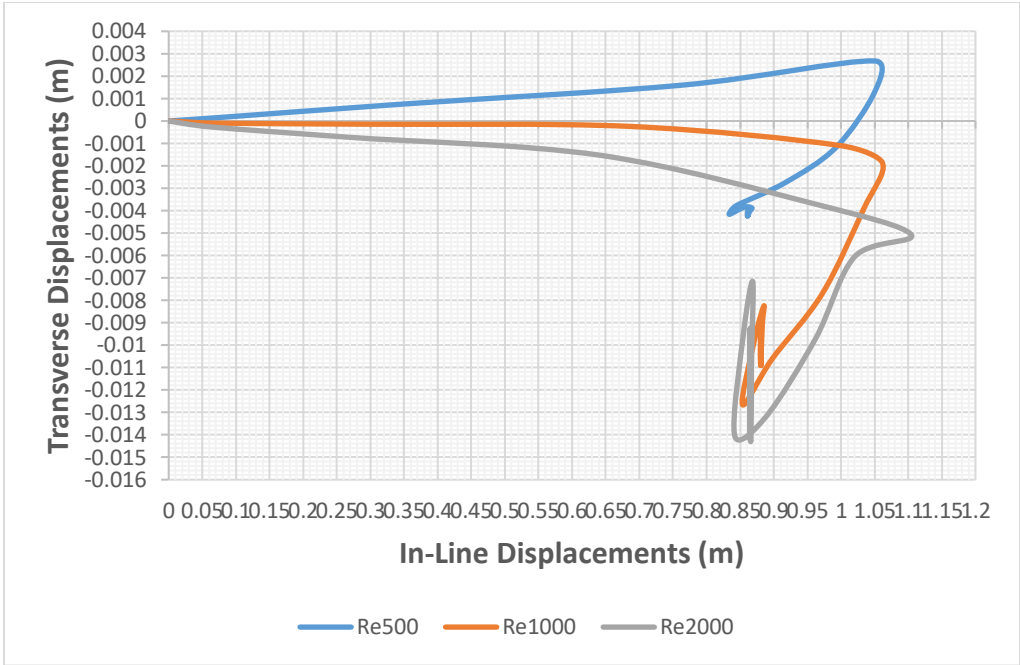
Figure 22. Overall displacement history of Re500, 1000, and 2000.
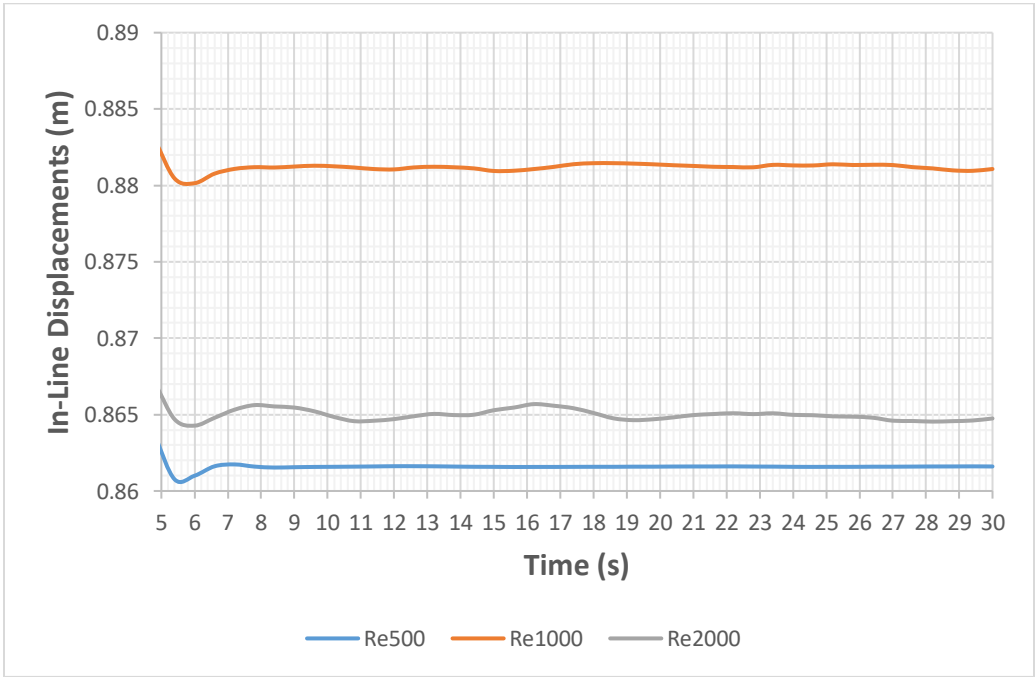
Figure 23. Re500, 1000, and 2000 in-line displacements versus time
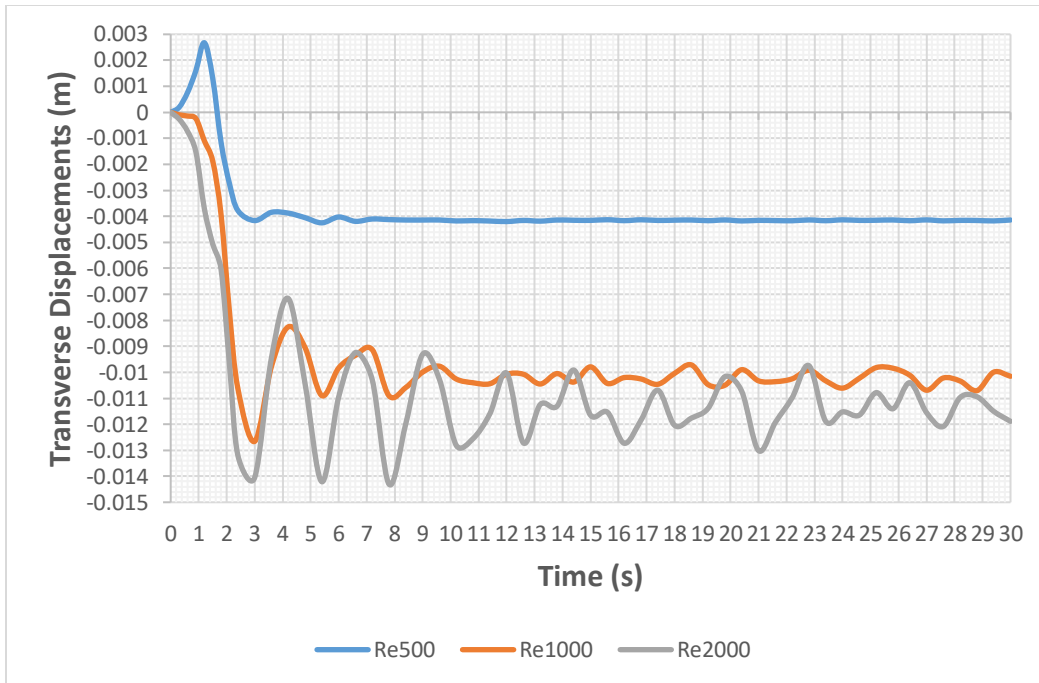
Figure 24. Re500, 1000, and 2000 transverse displacements versus time

There are more investigations of five deformable models in the next section, including lift and drag coefficients. Each Reynolds number corresponds to three simulations—FSI, flow past a rigid regular cylinder, and flow past a rigid deformed cylinder. The rigid deformed cylinder means the deformation of the cylinder is exported from FSI simulation and set rigid. The final deformation of Re500, Re1000, and Re2000 can be assumed steady. As for cases Re100 and Re300, because there are large vibrations in later periods, the deformation geometries are exported from the earlier (steady-state) stage.

3.2 Comparisons Between FSI and Rigid Model Tests

3.2.1 Reynolds number of 100
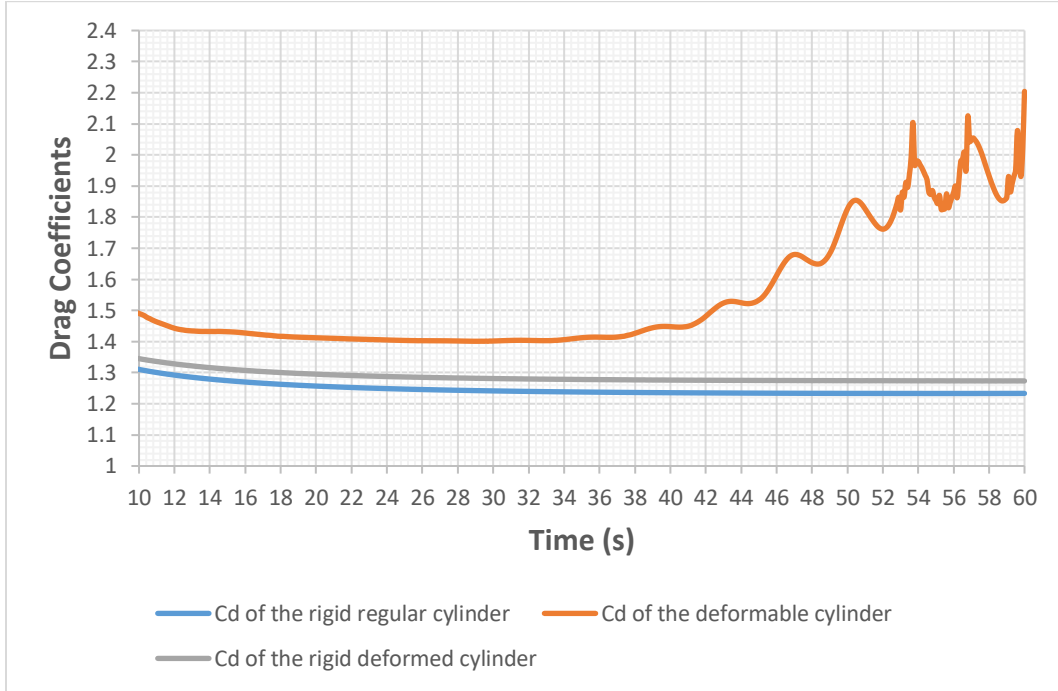
Figure 25. Drag coefficients of Re100

As shown in Figure 25, the coefficients of the rigid regular cylinder and the rigid deformed cylinder are close to each other, and the latter one is slightly bigger, which shows that the pre-strain of Re100 increases the drag force. As for the deformable cylinder, the drag coefficient is much larger than the others, and it exceedingly increases after 40 seconds with massive fluctuations. The displacement history of Re100 confirms these fluctuations. Thus, violent structural vibrations and vortex shedding increase drag and fluctuations. In return, the drag increase and fluctuations bring about large deformation and vibrations.
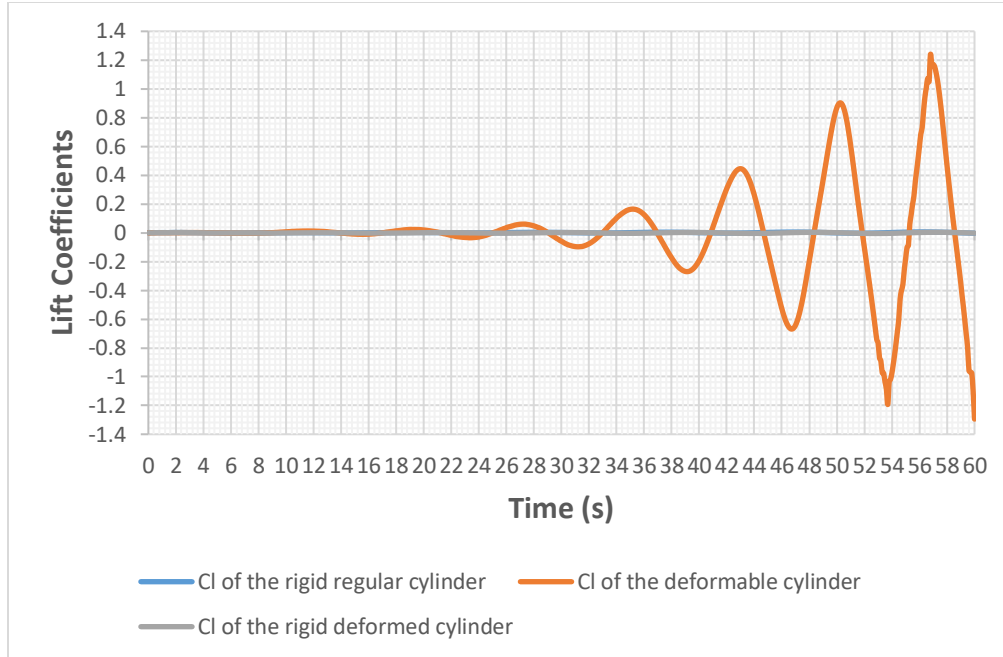
Figure 26. Lift coefficients of Re100

Compared with the lift coefficient of the deformable cylinder, lift coefficients of the rigid regular cylinder and rigid deformed cylinder are approximately zero, as seen in Figure 26. The variation frequency of the orange curve is 0.133 Hz, and it is precisely the vortex shedding and structural vibration frequency. Due to VIVs of Re100, drag and lift forces dramatically increase. If such forces unboundedly grow, the whole structure will eventually fail. Alternatively, the growth might be controlled under damping force and stay at a certain interval, but alternating stress still might cause fatigue cracks.
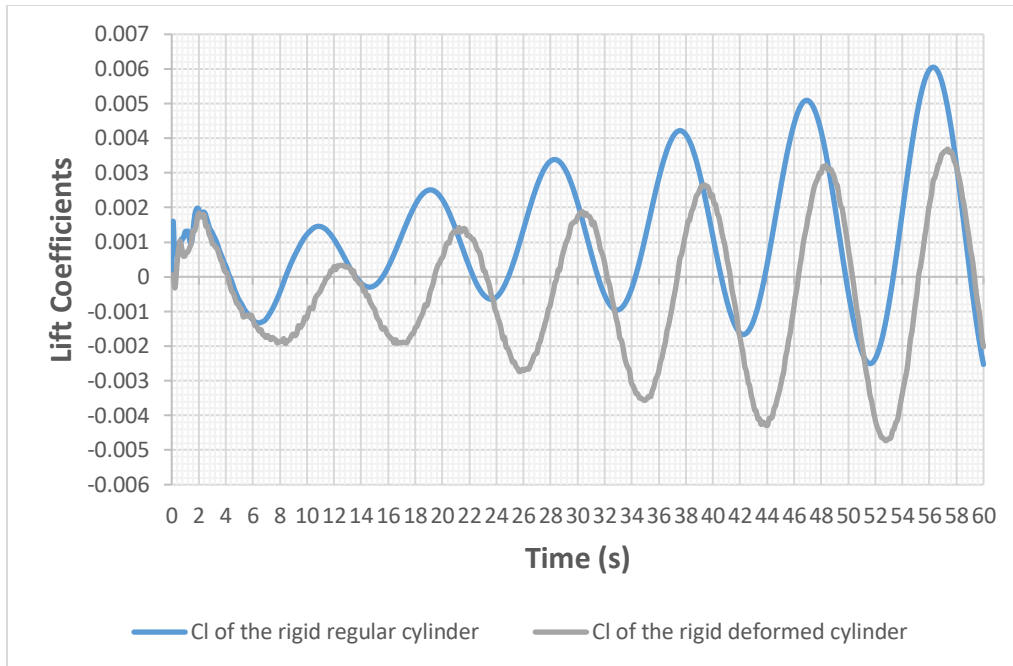
Figure 27. Zoomed-In lift coefficients of Re100

Figure 27 demonstrates the zoomed-in statistics of the rigid regular cylinder and the rigid deformed cylinder. The zoom-in lift coefficients of the rigid deformed cylinder and the rigid regular cylinder are hundreds of times smaller than the lift coefficients of the deformable cylinder. The absolute amplitudes of these two groups are approximate; that is, the deformation of Re100 does not bring remarkable changes to lift coefficients.

3.2.2 Reynolds number of 300
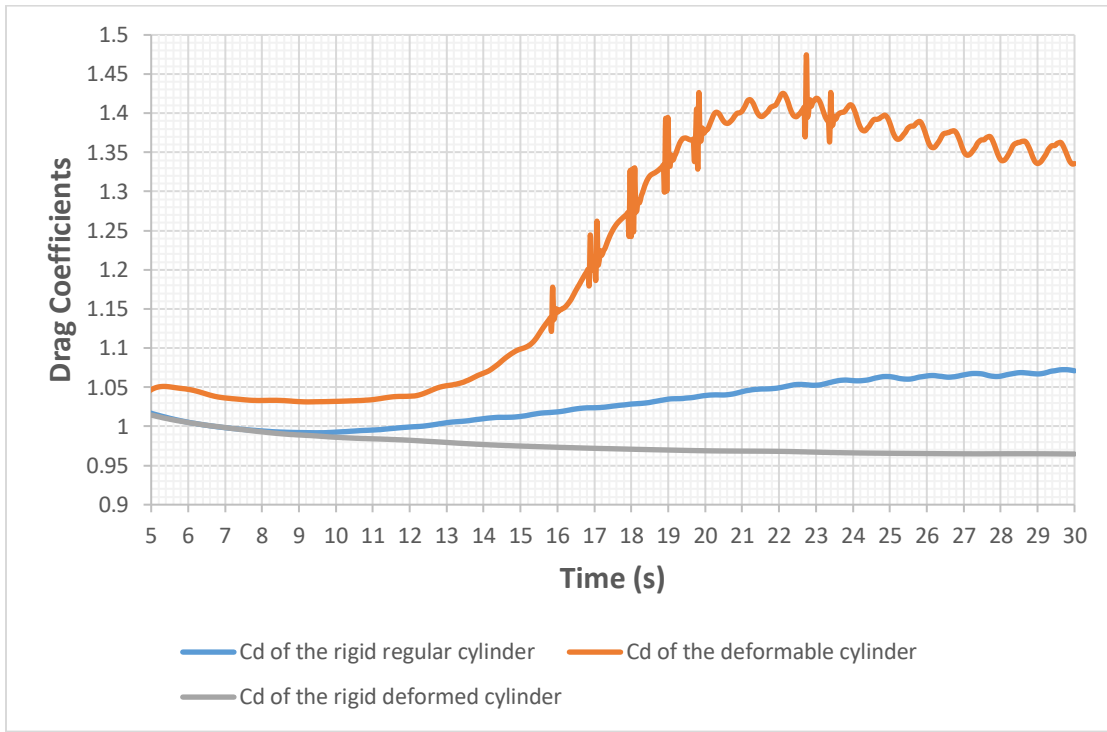
Figure 28. Drag coefficients of Re300

The chart above shows that drag coefficients of the rigid regular cylinder and rigid deformed cylinder are close to each other at the beginning. However, the Cd of the rigid deformed cylinder gradually drops to 0.96, 0.1 lower than the Cd of the rigid regular cylinder. In other words, the pre-strain decreases the drag force. In the FSI simulation, the drag coefficient quickly exceeds those of the rigid cylinder (deformed or regular). Notably, the Cd of the deformable cylinder dramatically increases up to 1.45 and fluctuates down to 1.35. It should be noted that there are several pikes and jagged patterns after 15 seconds, which means the cylinder is extremely unstable because of the VIVs, and the drag coefficient fluctuates remarkably within small timesteps. As mentioned before, the cylinder does not only vibrate but also distorts, contributing to drag increase and instability.

29
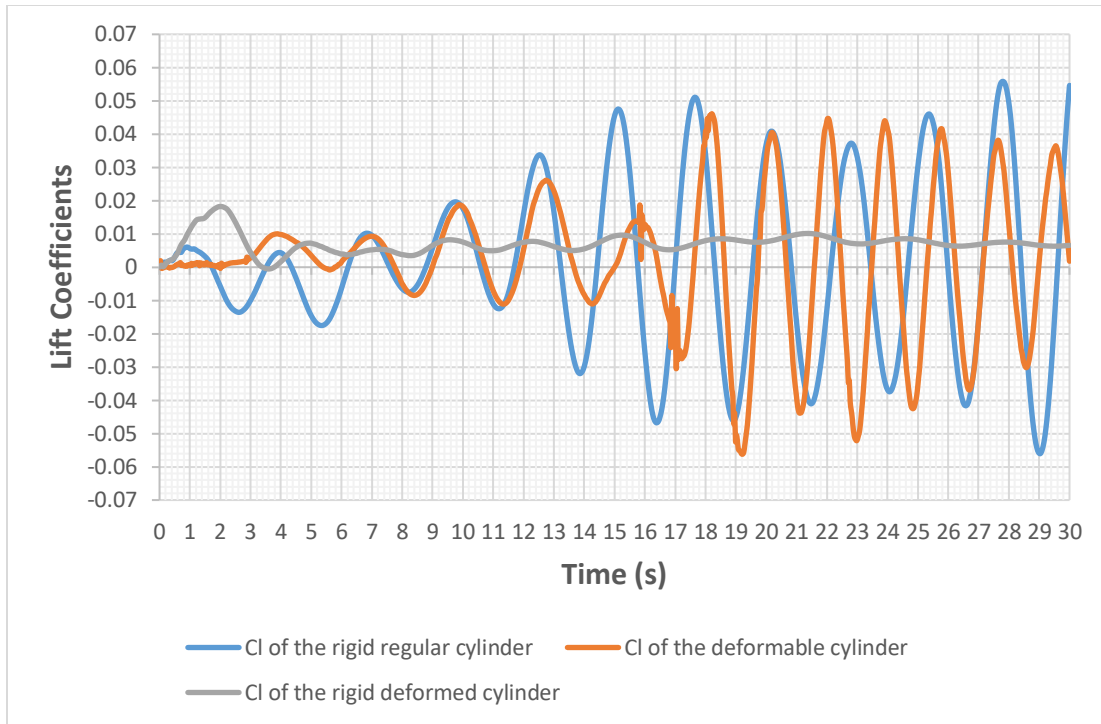
Figure 29. Lift coefficients of Re300

In Figure 29, the lift coefficients of the deformable cylinder and the rigid regular cylinder are nearly at the same level, even though they do not precisely coincide with each other. However, the Cl of the rigid deformed cylinder is much smaller. That said, deformation does bring about corresponding impacts to lift force. Indeed, transverse displacements of Re300 are much lower than that of Re100, and the lift coefficients of FSI Re100 and Re300 explain the reason. But there are still peaks and jagged in the figure above, during the interval 15–18 seconds of the deformable cylinder case.

3.2.3 Reynolds number of 500
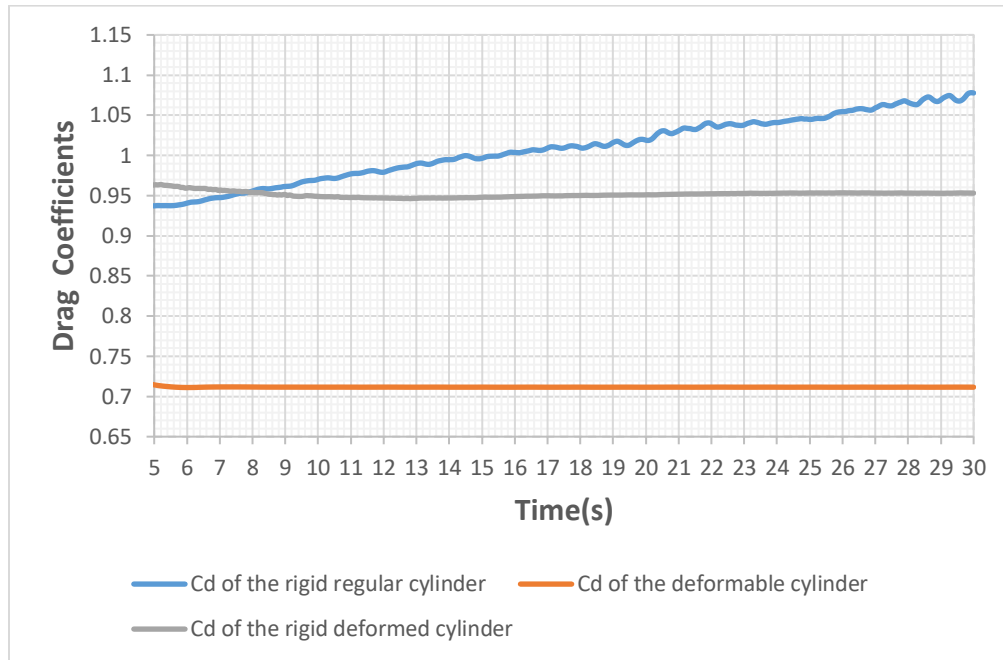
Figure 30. Drag coefficients of Re500

The chart above shows that the drag coefficient line of the deformable cylinder is much lower than the others and remains approximately 0.71 after 5 seconds. While the drag coefficient of the rigid deformed cylinder keeps 0.95 after 10 seconds, the rigid regular cylinder starts to mount above with local fluctuations. This phenomenon explains that vortices shedding increases drag and makes periodic drag fluctuations. Even though the rigid deformed cylinder takes advantage of pre-strain, and the drag coefficient is steady after 10 seconds, it is still higher than that of the deformable cylinder.

For flow around blunt bodies, pressure drag and skin friction drag dominate. Pressure drag is highly related to the shape of the body, so it is also called form drag. As the deformable cylinder has the same geometry as the rigid deformed cylinder, the pressure drag should be close. As a result, the lower resistance of the deformable cylinder attributes to the lower skin friction drag.

31
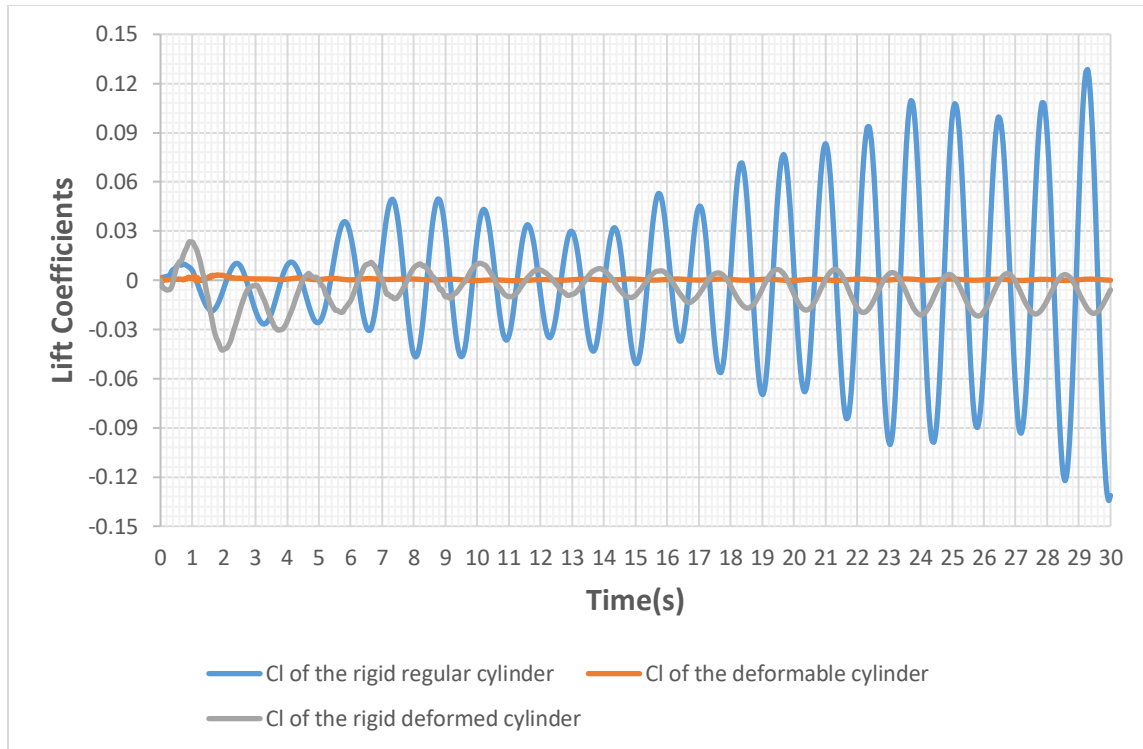
Figure 31. Lift coefficients of Re500

In Figure 31, it is quite clear that the lift coefficient amplitude of the rigid regular cylinder is much higher than that of the others. Again, periodic vortex shedding not only causes drag fluctuations but remarkably affects lift variations. The lift coefficient of the rigid deformed cylinder fluctuates to a relatively smaller amplitude than the rigid regular one because of the shape change. Last but not least, the lift coefficient of the deformable cylinder is around zero, even though it is not a straight line. From this perspective, it makes sense that the FSI simulation of the Re500 shows no vibrations or vortex shedding.

3.2.4 Reynolds number of 1000
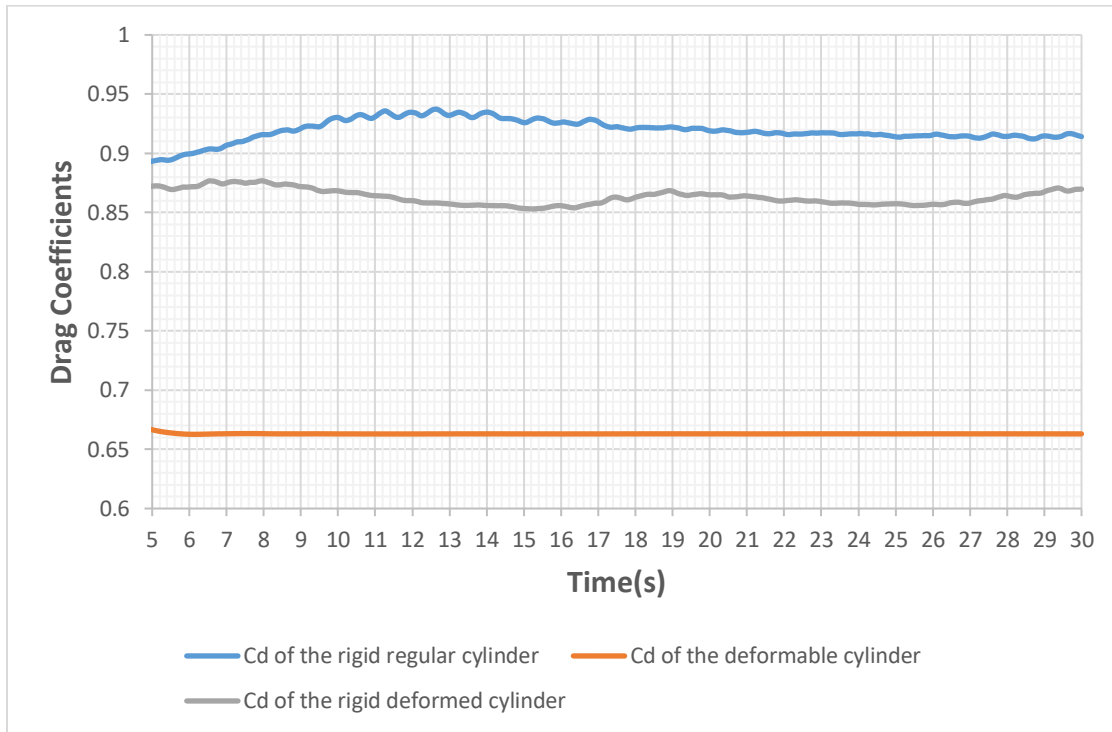
Figure 32. Drag coefficients of Re1000

As shown in Figure 32, the drag coefficient of the deformable cylinder is still at the lowest level and remains 0.66. However, unlike the chart of Re500, the drag coefficient of the rigid deformed cylinder fluctuates around 0.86. Also, the blue line fluctuates around 0.91. Even though the deformed cylinder mitigates vortex shedding to some degree, the flow is less steady because of the increase of the Reynolds number. That is why the Cd of the rigid deformed cylinder is not constant.
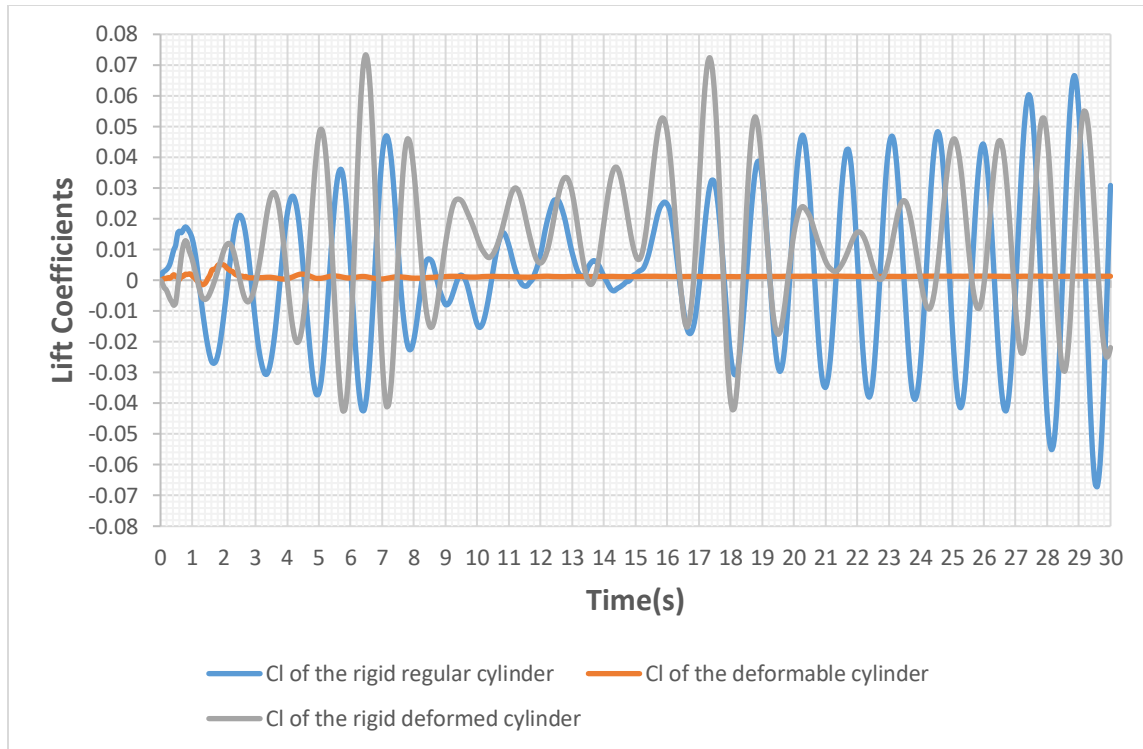
Figure 33. Lift coefficients of Re1000

As shown in Figure 33, the lift coefficient of the deformable cylinder is nearly zero, while the other two curves fluctuate wildly. This time, the amplitudes of grey and blue curves are approximately the same level. That is, the pre-strain effect is not as sufficient as that of Re500 and causes alternating lift force. If we compare the lift coefficients of the deformable cylinder and the rigid deformed cylinder, we would conclude another critical factor that influences lift force: rigidity. As we mentioned before, the final deformation of Re500, Re1000, and Re2000 FSI are assumed to be steady, so the pre-strain is the same under the same Reynolds number. Thus, flexibility brings a tiny amount of deformation that can balance the lift to approximately zero.

3.2.5 Reynolds number of 2000
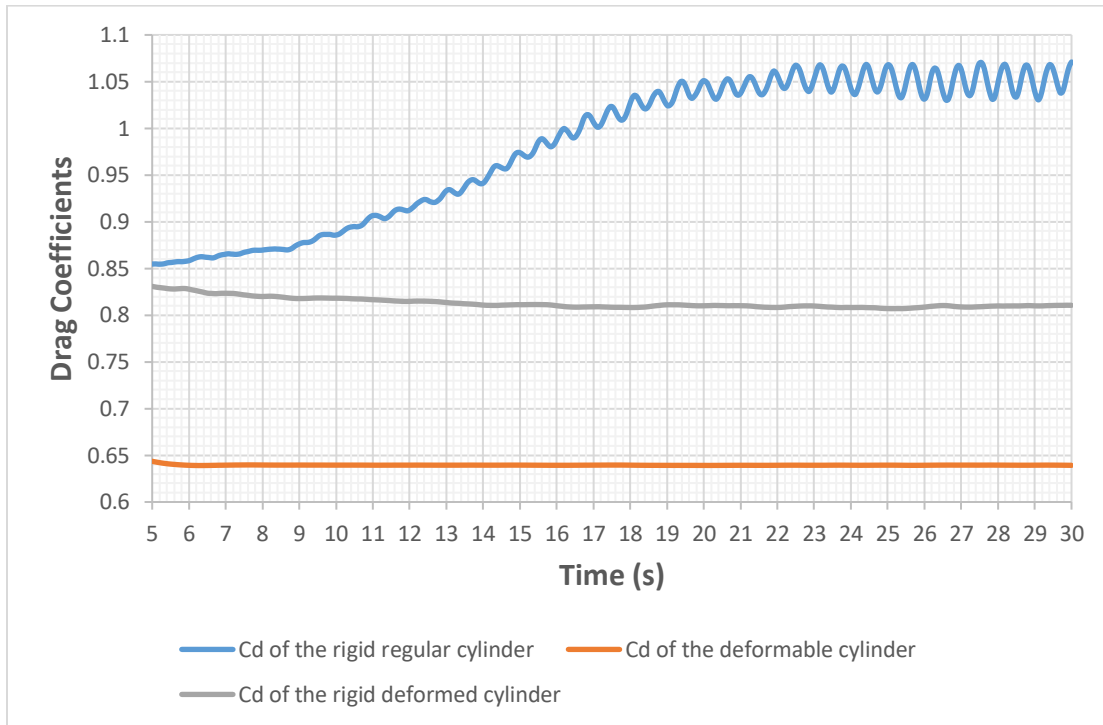
Figure 34. Drag coefficients of Re2000

In Figure 34, the drag coefficient of the deformable cylinder remains the smallest one and does not change after 6 seconds. Because of the deformation, the grey line is almost parallel to the orange one. The drag coefficient of the rigid regular cylinder gradually increases and fluctuates around 1.05 because of vortex shedding. It should be highlighted that the pre-stain of the cylinder decreases by a 0.35 drag coefficient, which is intriguing in industrial applications, such as anti-drag and system stability.

Figure 35. Lift coefficients of Re2000

In Figure 35, the blue curve dominates the others, and the orange one keeps zero while the grey line slightly fluctuates around zero. As the Reynolds number increases, vortex shedding significantly influences lift and drag coefficients of the rigid regular cylinder, and the lift is more sensitive because of the vortex shedding pattern—upper and lower spots behind the cylinder.
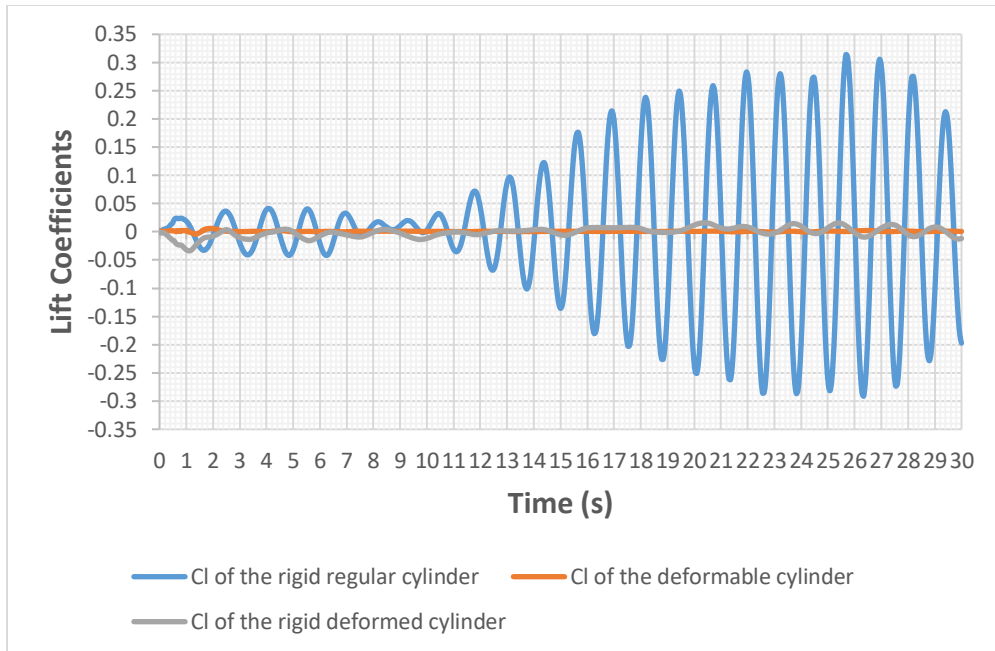
To summarize, drag and lift coefficients of FSI Re100 and Re300 are significantly larger than those of rigid tests as there are vortex-induced vibrations. The pre-stain does not work well, reducing drag and lift. However, in the last three cases, no evident VIVs exist, so all drag and lift coefficients of FSI are much smaller than those of rigid tests. Besides, pre-stain decreases drag and lift coefficients to different degrees. The relative roughness is another important factor of drag and deserves future attention.

Recall that in the FSI simulations of Re500, Re1000, and Re2000, most of the fluid domain is steady. Pre-strain is one of the reasons, but another factor, rigidity of the structure, demonstrates its contribution in Figures 36–38.
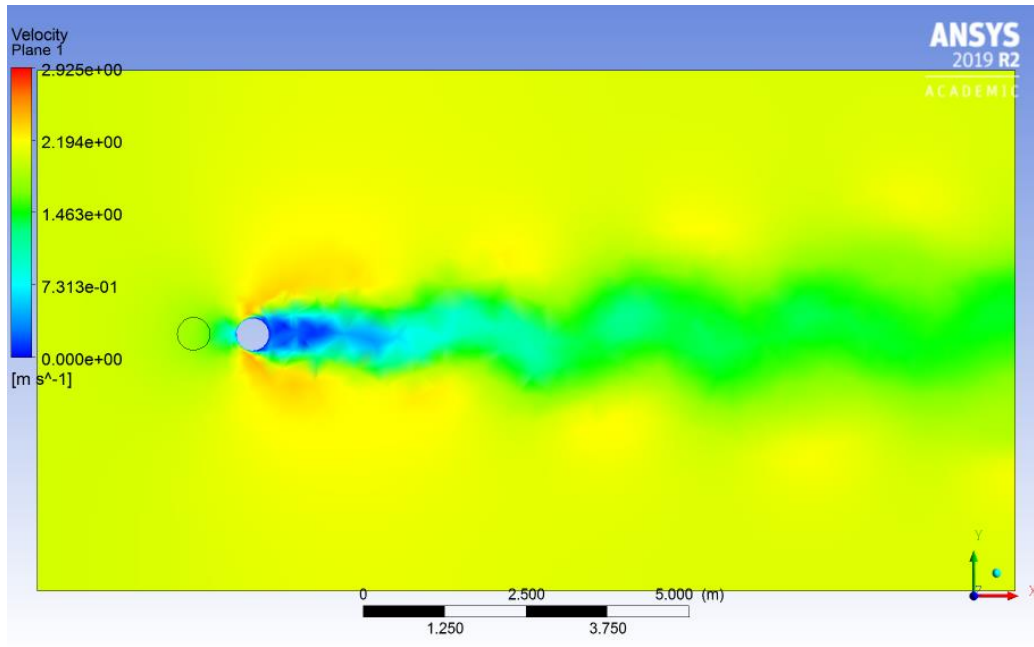
Figure 36. Re500 of flow past the rigid deformed cylinder
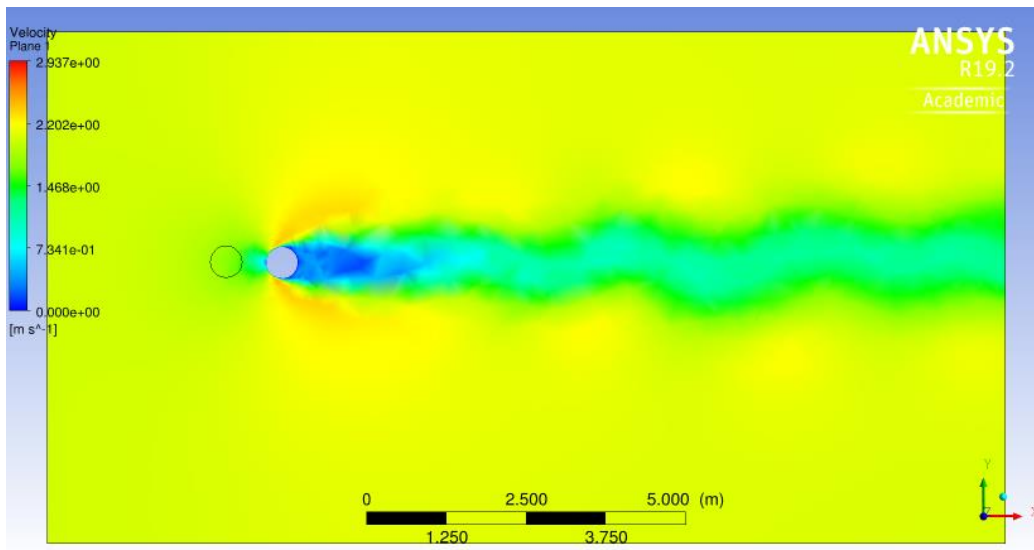
Figure 37. Re1000 of flow past the rigid deformed cylinder
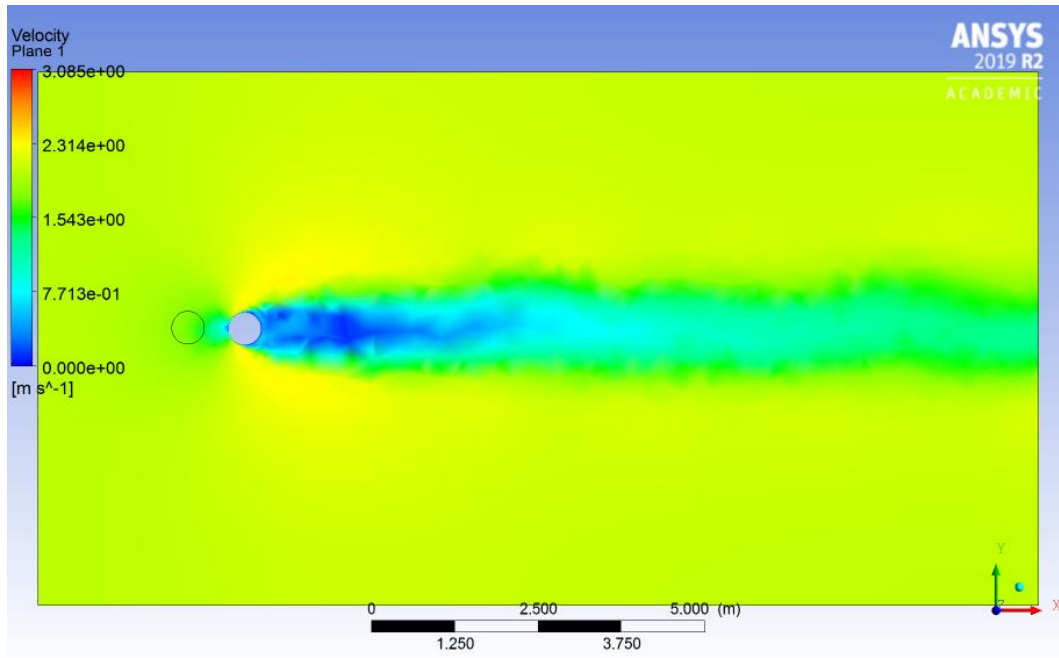
Figure 38. Re2000 of flow past the rigid deformed cylinder

As we said before, pre-strain decreases drag and lift force and mitigates vortex shedding to some degree in Re500, Re1000, and Re2000. But it is not enough because we can still see the vortex shedding or wake oscillations in the pictures above. The difference between FSI flow past a rigid deformed cylinder is that small deformation is allowed in FSI even though the structure is assumed to be steady. Such small deformation yields to the flow and mitigates or prevents wake oscillations or vortex shedding.

4.0 Conclusions

In this paper, we visualized the phenomena of VIVs and bifurcations to displacements record and analyzed lift and drag coefficients. The complicated mechanism of VIVs involves multiple parameters, such as the Reynolds number, mass ratio, rigidity, structural frequency, and so on. We studied several significant factors, and here are the concluding remarks.

Resonance is demonstrated to be the crucial factor of VIVs in the FSI Re100 and Re300 even though the energy of the flow is smaller than that of Re500. Thus, we should test and avoid coinciding structural frequency with vortex shedding frequency—for example, by changing fixed support, length, or geometry of the structure.

The Reynolds number may not be specific enough to represent the characteristic of both flow and structure because of the existence of FSI. Even though the Reynolds numbers are the same, the structural forces could still be different, due to velocity and viscosity's contribution to drag force. As a result, different deformations relate to different vibration modes that have already been demonstrated in our experiments. It also makes sense from the resonance perspective; velocity is related to vortex shedding frequency while viscosity is not, and dimensional lengths and fixed modes also determine the structural frequency. Thus, in future research, we need to investigate these different aspects to understand what is the most significant part of VIVs.

In the five groups of FSI experiments, three pre-strains (Re500, 1000, 2000) help mitigate or prevent vortex shedding, and four groups of pre-strains (Re300, 500, 1000, 2000) contribute drag decrease in flow past rigid deformed cylinder tests. Appropriate pre-strain of the cylinder is effective in decreasing drag, mitigating vortex shedding under a specific range of Reynolds numbers. For FSI simulations, there are different stages (Re100 and Re300; Re500; Re1000 and

Re2000) and two bifurcations (transient to steady, and steady to transient). The whole fluid domain is transient, such as Re100 and Re300; the entire fluid domain is almost steady for Re500; compared with Re500, more and more domain is transient for Re1000 and Re2000, and there are perceivable vibrations in Re2000.

Rigidity or flexibility of the structure plays a significant role in balancing lift, and the small deformation in FSI Re500, Re1000, and Re2000 decreases the absolute value of lift coefficients to nearly zero. Cooperating with the pre-strain, the flexibility of the silicon rubber successfully mitigates or prevents the vortex shedding if there is no resonance.

Other details, such as how the flow domain far from the middle of the cylinder is more vibrant in FSI simulations and relative roughness is crucial in drag decrease, should also be developed in future research.

Bibliography

Bearman, P. W., & Owen, J. C. (1998). Reduction of bluff-body drag and suppression of vortex shedding by the introduction of wavy separation lines. *Journal of Fluids and Structures*. https://doi.org/10.1006/jfls.1997.0128

Coutanceau, M., & Defaye, J. R. (1991). Circular cylinder wake configurations:A flow visualization survey. *Applied Mechanics Reviews*. https://doi.org/10.1115/1.3119504

Currie, I. G., & Currie, I. G. (2002). *Fundamental Mechanics of Fluids, Third Edition*. Retrieved from https://books.google.com/books?id=EbQgtwAACAAJ

Gabbai, R. D., & Benaroya, H. (2005). An overview of modeling and experiments of vortex-induced vibration of circular cylinders. *Journal of Sound and Vibration*, *282*(3–5), 575–616. https://doi.org/10.1016/j.jsv.2004.04.017

Govardhan, R. N., & Williamson, C. H. K. (2006). Defining the "modified Griffin plot" in vortex-induced vibration: Revealing the effect of Reynolds number using controlled damping. *Journal of Fluid Mechanics*. https://doi.org/10.1017/S0022112006000310

Griffin, O. M., Skop, R. A., & Ramberg, S. E. (1975). The resonant, vortex-excited vibrations of structures and cable systems. *Proceedings of the Annual Offshore Technology Conference*.

Grunwald, G. (1989). Chen, S.-S., Flow-Induced Vibration of Circular Cylindrical Structures. Washington etc., Hemisphere Publishing Corporation. Berlin etc., Springer-Verlag 1987. XXV, 464 pp., 204 figs., DM 168,–. ISBN 3-540-17956-9. *ZAMM - Journal of Applied Mathematics and Mechanics / Zeitschrift Für Angewandte Mathematik Und Mechanik*. https://doi.org/10.1002/zamm.19890690117

Logan, D. L., Veitch, E., Carson, C., Burrell, K. R., Gould, V., Wagner, E., … Wagner, E. (2007). A First Course in the Finite Element Method Fourth Edition. In *Transport*. https://doi.org/10.1016/0022-460X(91)90505-E

Navrose, N., & Mittal, S. (2016). Lock-in in vortex-induced vibration. *Journal of Fluid Mechanics*, *794*, 565–594. https://doi.org/10.1017/jfm.2016.157

Owen, J. C., Bearman, P. W., & Szewczyk, A. A. (2001). Passive control of VIV with drag reduction. *Journal of Fluids and Structures*. https://doi.org/10.1006/jfls.2000.0358

Raissi, M., Wang, Z., Triantafyllou, M. S., & Karniadakis, G. E. (2019). Deep learning of vortex-induced vibrations. *Journal of Fluid Mechanics*, *861*, 119–137. https://doi.org/10.1017/jfm.2018.872

Schulz, K. W., & Kallinderis, Y. (1998). Unsteady Flow Structure Interaction for Incompressible Flows Using Deformable Hybrid Grids. *Journal of Computational Physics*, *143*(2), 569–597. https://doi.org/10.1006/jcph.1998.5969

Shoele, K., & Zhu, Q. (2010). Flow-induced vibrations of a deformable ring. *Journal of Fluid Mechanics*, *650*, 343–362. https://doi.org/10.1017/S0022112009993697

Sun, X., Wang, S. Z., Zhang, J. Z., & Ye, Z. H. (2018). Bifurcations of vortex-induced vibrations of a fixed membrane wing at Re ≤ 1000. *Nonlinear Dynamics*, *91*(4), 2097–2112. https://doi.org/10.1007/s11071-017-4004-1

Tombazis, N., & Bearman, P. W. (1997). A study of three-dimensional aspects of vortex shedding from a bluff body with a mild geometric disturbance. *Journal of Fluid Mechanics*. https://doi.org/10.1017/S0022112096003631

Tu, J., Yeoh, G. H., & Liu, C. (2018). Computational fluid dynamics: A practical approach. In *Computational Fluid Dynamics: A Practical Approach*.

Vikestad, K., Vandiver, J. K., & Larsen, C. M. (2000). Added mass and oscillation frequency for a circular cylinder subjected to vortex-induced vibrations and external disturbance. *Journal of Fluids and Structures*. https://doi.org/10.1006/jfls.2000.0308

Wang, S., Khoo, B. C., Liu, G. R., Xu, G. X., & Chen, L. (2014). Coupling GSM/ALE with ES-FEM-T3 for fluid-deformable structure interactions. *Journal of Computational Physics*, *276*, 315–340. https://doi.org/10.1016/j.jcp.2014.07.016

Williamson, c. (1996). Vortex Dynamics in the Cylinder Wake. *Annual Review of Fluid Mechanics*. https://doi.org/10.1146/annurev.fluid.28.1.477

Yeung, R. W., & Vaidhyanathan, M. (1993). Flow past oscillating cylinders. *Journal of Offshore Mechanics and Arctic Engineering*. https://doi.org/10.1115/1.2920112

Zdravkovich, M. M. (1981). Review and classification of various aerodynamic and hydrodynamic means for suppressing vortex shedding. *Journal of Wind Engineering and Industrial Aerodynamics*. https://doi.org/10.1016/0167-6105(81)90036-2